

# Application of Mellin Kind Statistics to Polarimetric G Distribution for SAR Data

Salman Khan, *Student Member, IEEE*, and Raffaella Guida, *Member, IEEE*

**Abstract**—The  $\mathcal{K}$  distribution can be arguably regarded as one of most successful and widely used models for radar data. However, in the last two decades we have seen tremendous growth in even more accurate modeling of radar statistics. In this regard, the relatively recent  $\mathcal{G}^0$  distribution filled some deficiencies left unaccounted by the  $\mathcal{K}$  model. The  $\mathcal{G}^0$  model actually resulted as a special case of a more general model; the  $\mathcal{G}$  distribution, which also has the  $\mathcal{K}$  model as its special form. Singlelook complex (SC) and multilook complex (MC) polarimetric extensions of these models (and many others) have also been proposed in this prolific era. Unfortunately, statistical analysis using the polarimetric  $\mathcal{G}$  distribution remained limited, primarily because of more complicated parameter estimation. In this paper, the authors have analyzed the  $\mathcal{G}$  model for its parameter estimation using state-of-the-art univariate and matrix-variate Mellin Kind Statistics (MKS). The outcome is a class of estimators based on Method of Log Cumulants (MoLC), and Method of Matrix Log Cumulants (MoMLC). These estimators show superior performance characteristics for product model distributions like the  $\mathcal{G}$  model. Diverse regions in TerraSAR-X polarimetric SAR (PolSAR) data have also been statistically analyzed using the  $\mathcal{G}$  model with its new and old estimators. Formal Goodness-of-fit (GoF) testing, based on MKS theory, has been used to assess the fitting accuracy between different estimators and also between  $\mathcal{G}$ ,  $\mathcal{K}$ ,  $\mathcal{G}^0$ , and Kummer- $\mathcal{U}$  models.

**Index Terms**—synthetic aperture radar (SAR), polarimetric G distribution, generalized inverse gaussian (GIG), Fisher, Kummer-U distribution, radar statistics, Mellin kind statistics, Method of log cumulants, numerical differentiation

## I. INTRODUCTION

**O**BJECTS illuminated by light from a highly coherent continuous wave laser are readily observed to acquire a peculiar granular appearance called *speckle*. The origins of speckle were promptly recognized by early researchers in the laser field [1]. Direct analogs of speckle are found in all types of coherent imagery including SAR. One intuitive explanation of speckle formation in coherent imagery is that the reflected waves from different scatterers arrive back at the source with random delays. The incoherent addition of these out-of-phase reflected components results in chaotic bright and dark spots [2]. Due to the random nature of speckle, SAR imagery is inherently probabilistic. Consequently, statistical modeling of SAR data is a fundamental aspect of SAR image analysis.

Let us make the following assumptions 1) a large number of scatterers are present in a resolution cell, 2) the slant range is much larger than the wavelength, 3) the amplitude and phase from individual scatterers are independent and identically distributed random variables, and 4) the phase is uniformly distributed. Then, according to central limit theorem, the complex return from a singlelook complex (SC) SAR image follows a zero mean circular complex gaussian distribution [3]. The

gaussian model also includes the corresponding distributions of singlelook (and multilook) amplitude and intensity returns. It can be readily derived, that the corresponding singlelook amplitude is Rayleigh distributed, while the singlelook intensity is exponentially distributed [3]. For multilook data, the amplitude is square root of gamma distributed, while the intensity is gamma distributed [3]–[5]. It has been experimentally verified that the gaussian model generally provides a good fit to singlelook and multilook SAR data specially when the image roughness is relatively low and a large number of scatterers are present. As the resolution increases, the assumption of a large number of scatterers in a resolution cell is not always true. It has also been noted that in certain areas of a SAR image the statistics deviate from the gaussian assumption e.g. urban areas show considerable non-gaussianity [6], [7]. Similarly, natural areas like forests and rough sea surface are also known to exhibit non-gaussianity [8], [9].

Many distributions have been proposed to model non-gaussianity for single-channel SAR data e.g. Weibull, Log-normal, Nakagami-Rice [7]. However, some distributions have been derived for single-channel as well as multi-channel (PolSAR) data using a doubly stochastic product model. This model provides a framework to generate multivariate non-gaussian distributions by assuming that the observed signal is a product of a gaussian speckle random variate and a non-gaussian *texture* random variate. A special case of this model, called *scalar texture product model*, has been extensively and successfully used to model non-gaussianity for single-channel and more importantly PolSAR data. This model assumes that the texture random variate is restricted to a positive scalar random variable. The extension to PolSAR data is not straightforward as noted in [4], and mandates certain assumptions. Recently, some research has been done in multi-texture modeling as well [10], [11]. In this paper, we will restrict ourselves to the scalar texture case as our methods are scalable to certain multi-texture cases. In contrast to contemporary literature, we will use the terms *textured* and *textureless* areas when we refer to areas with non-gaussian and gaussian statistics, respectively<sup>1</sup>.

Singlelook PolSAR speckle can be shown to follow a multivariate zero mean complex gaussian distribution [12]. The gaussian counterpart for the multilook PolSAR case is the matrix-variate scaled complex Wishart distribution [12]. Both these models have been experimentally verified on real PolSAR data [13], [14]. In the context of scalar texture product model, different distributions for the texture random

<sup>1</sup>gaussian and non-gaussian areas have been commonly referred to as homogeneous and heterogeneous areas, respectively. We refrain from this nomenclature as some homogeneous areas also show non-gaussianity.

variable will result in different expressions for the resulting *compound distribution*. The choice of texture distribution can be based on physical characteristics, empirical evidence, or simply flexibility of fitting real data. Some of the important texture distributions proposed in literature are gamma ( $\gamma$ ), inverse gamma ( $\gamma^{-1}$ ), Generalized Inverse Gaussian (GIG), Fisher<sup>2</sup> ( $\mathcal{F}$ ), beta ( $\beta$ ), and inverse beta ( $\beta^{-1}$ ) with the resulting compound distributions  $\mathcal{K}$ ,  $\mathcal{G}^0$ ,  $\mathcal{G}$ , Kummer- $\mathcal{U}$ ,  $\mathcal{W}$ , and  $\mathcal{M}$ , respectively [6], [18]–[24]. All the compound distributions have certain special functions in their closed form expressions. Generally, the less complicated the special function, and the more flexible the distribution shape, the better. In this regard, the  $\mathcal{G}^0$  distribution has been shown to be very flexible and computationally inexpensive, capable of modeling varying degrees of texture [6], [21]. However, real PolSAR data in various frequency bands often requires more flexibility than the  $\mathcal{G}^0$  model [22]–[25]. This paper concentrates on the  $\mathcal{G}$  distribution, a very flexible model, derived assuming GIG texture, with  $\mathcal{K}$  and  $\mathcal{G}^0$  distributions as its well known special cases [6], [21], [25]. Recently, it has also been shown by the authors that this model is at least as flexible as the Kummer- $\mathcal{U}$  distribution [11]. It is also pertinent to mention, that the  $\mathcal{G}$  distribution has another special case referred to as the harmonic  $\mathcal{G}$  distribution, denoted as  $\mathcal{G}^h$ , proposed for single-channel case in [26], and extended to model multilook complex (MC) polarimetric data in [27], and SC polarimetric data in [28]<sup>3</sup>.

Efficient parameter estimation of the polarimetric  $\mathcal{G}$  distribution has been a hard computational task [6], [21], [25]. One alternative is to estimate parameters on each individual channel, and average the so called *mono-pol* estimates to obtain estimates for the polarimetric distribution (See Section III). Such mono-pol estimators have been shown to be inferior, in terms of estimator bias and variance, to polarimetric estimators<sup>4</sup> [29]. An important development in this regard has been the MoLC for mono-pol parameter estimation [15], which has been extended to polarimetric estimators in [29], [30]. The MoLC estimation has been shown to be suitable and intuitive for compound distributions (mono-pol and polarimetric) arising from the doubly stochastic product model [15], [24], [29], [30].

In this paper, we apply the MoLC estimation to the polarimetric singlelook and multilook  $\mathcal{G}$  distribution, extending our preliminary work presented in [11]. Then, we compare the new polarimetric estimator to two other somewhat traditional estimators: 1) based on mono-pol fractional moments, and 2) numerical Maximum Likelihood Estimation (MLE) [25], extended to the multilook case. Further, we apply all the above

mentioned estimators for  $\mathcal{G}$  distribution to real PolSAR data. Also, we apply the polarimetric MoLC estimators for  $\mathcal{G}^0$ ,  $\mathcal{K}$ , and Kummer- $\mathcal{U}$  distributions to real PolSAR data [29], [30]. Finally, we compute a formal  $\chi^2$  distributed Goodness-of-Fit (GoF) test statistic, based on multiple log cumulants and specially designed for polarimetric data [31]. This facilitates the GoF comparison between different estimators and distributions on real data.

The rest of the paper has been organized as follows. Section II elaborates the scalar texture product model for single-channel intensity and polarimetric SC and MC SAR data formats. Section III presents the  $\mathcal{G}$  distribution corresponding to these formats. Previously known estimators of the  $\mathcal{G}$  distribution are also listed in Section III. In Section IV, a brief review of MKS is documented as an essential prerequisite to MoLC. Section V covers the MoLC for the above mentioned SAR data formats. Univariate MKS theory has been applied to GIG pdf in Section VI. Close form expressions for log cumulants of  $\mathcal{G}$  distribution are listed in Section VII. In Section VIII, the proposed estimator's accuracy and precision are compared to those of the known estimators. Section IX briefly describes the GoF framework. Section X shows the application to real PolSAR data. Finally, in Section XI some conclusions are drawn.

## II. THE SCALAR TEXTURE PRODUCT MODEL

The scalar texture product model, as mentioned before, states that the observed signal is a product of a positive scalar texture random variable and a speckle random variate. The former is analogous to the natural spatial variation of radar cross section, which generally varies even for thematically similar pixels. It is also assumed that the texture is spatially varying on a larger scale than speckle. The product model takes different forms for SC and MC PolSAR data formats. This is because MC data contains all the second order moments of the scattering coefficients of SC data within a multilook window [32]. Hence, the statistics of these data formats are different. In the following, we assume  $\tau$  to represent a positive scalar texture random variable with an unspecified pdf  $p_\tau(\tau)$ . We also assume that the speckle random variate is normalized so that the scale is transferred to the texture variable, and hence its scale parameter must be separately estimated.

### A. Single-channel Intensity Return

First we consider the case of mono-pol intensity return. The product model is thus given by:

$$I = \tau x \quad (1)$$

where  $I$  is the intensity return, and  $x$  is the speckle intensity random variable. The pdf of  $x$  is exponentially distributed for singlelook case and  $\gamma$  distributed for multilook case. As exponential distribution is a special form of the  $\gamma$ , it is sufficient to show only the distribution of multilook intensity speckle [5]:

$$p_x\left(x; L, \frac{\sigma^2}{L}\right) = \left(\frac{L}{\sigma^2}\right)^L \frac{x^{L-1}}{\Gamma(L)} \exp\left(-\frac{Lx}{\sigma^2}\right), \quad (2)$$

<sup>2</sup>It is relevant to mention, that the  $\mathcal{F}$  distribution, proposed by Nicolas, 2002 [15], [16] to model texture and also intensity [17], is only the  $\mathcal{G}_I^0$  intensity distribution parameterised by its mean, proposed earlier by Frery et al., 1997 [6]. Both result from the product of  $\gamma$  and  $\gamma^{-1}$  distributed random variables. However, the latter was proposed only for intensity return, while the former modeled both texture and intensity.

<sup>3</sup>In [28], the SC polarimetric  $\mathcal{G}^h$  distribution was referred to as multivariate normal inverse gaussian (MNIG) distribution.

<sup>4</sup>Polarimetric estimators utilize fully polarimetric information in the form of covariance structure between polarimetric channels for estimation unlike mono-pol estimators.

where  $L$  (number of looks) is the shape parameter,  $\frac{\sigma^2}{L}$  is the scale parameter,  $\sigma^2 = \mathbf{E}\{x\}$  is the mean speckle intensity, and  $\mathbf{E}\{\cdot\}$  is the expectation. Since speckle is considered normalised, it follows:

$$\sigma^2 = 1, \quad (3)$$

$$\Rightarrow \mathbf{E}\{I\} = \mathbf{E}\{\tau\}. \quad (4)$$

### B. Singlelook Complex Polarimetric Scattering Vector

The product model for SC polarimetric data is based on further assuming that the texture in all polarimetric channels is the same. The SC polarimetric scattering vector  $\mathbf{k}$  is defined as:

$$\mathbf{k} = \begin{bmatrix} s_{hh} & s_{hv} & s_{vh} & s_{vv} \end{bmatrix}^T \quad (5)$$

where  $s_{xy}$  represents the complex scattering coefficient with  $x$  as transmit,  $y$  as receive polarization (h-horizontal, v-vertical), and  $[\cdot]^T$  represents the transpose. The SC polarimetric product model is given by:

$$\mathbf{k} = \sqrt{\tau} \mathbf{x} \quad (6)$$

where  $\mathbf{x}$  is a  $d$  dimensional speckle vector, which follows a zero mean multivariate complex gaussian distribution, denoted as  $\mathbf{x} \sim \mathcal{N}_d^{\mathbb{C}}(\mathbf{0}, \mathbf{\Sigma})$ , where  $\mathbf{\Sigma} = \mathbf{E}\{\mathbf{x}\mathbf{x}^H\}$  is the covariance matrix of  $\mathbf{x}$ , and  $(\cdot)^H$  represents the Hermitian i.e. conjugate transpose. The pdf is given by [12]:

$$p_{\mathbf{x}}(\mathbf{x}; \mathbf{\Sigma}) = \frac{1}{\pi^d |\mathbf{\Sigma}|} \exp(-\mathbf{x}^H \mathbf{\Sigma}^{-1} \mathbf{x}), \quad (7)$$

where  $|\cdot|$  represents the determinant, and  $\mathbf{\Sigma}$  is computed using the sample covariance matrix (SCM),  $\mathbf{\Sigma}_{\text{SCM}}$ , as follows:

$$\mathbf{\Sigma}_{\text{SCM}} = \mathbf{E}\{\mathbf{k}\mathbf{k}^H\} = \mathbf{E}\{\tau\} \mathbf{E}\{\mathbf{x}\mathbf{x}^H\} = \mathbf{E}\{\tau\} \mathbf{\Sigma} \Rightarrow \mathbf{\Sigma} = \frac{\mathbf{\Sigma}_{\text{SCM}}}{\mathbf{E}\{\tau\}}. \quad (8)$$

It is normalized as in [28], such that:

$$|\mathbf{\Sigma}| = 1, \quad (9)$$

$$\Rightarrow \mathbf{E}\{\tau\} = |\mathbf{\Sigma}_{\text{SCM}}|^{\frac{1}{d}}, \quad (10)$$

and ensures that  $\mathbf{\Sigma}$  contains only polarimetric covariance structure information.

### C. Multilook Complex Polarimetric Covariance Matrix

Multilooking of single-channel SAR data discards all the phase information and results in real valued amplitude or intensity data. However, multilooking of PolSAR data retains the mean phase difference between the channels and produces complex data called MC [33]. The polarimetric multilooking operation is given by:

$$\mathbf{C} = \frac{1}{L} \sum_{l=1}^L \mathbf{k}_l \mathbf{k}_l^H, \quad (11)$$

where  $\mathbf{C} \in \Omega_+ \subset \mathbb{C}^{d \times d}$  is the multilook polarimetric covariance matrix. Note that  $\mathbf{C}$  is a random matrix defined on the cone,  $\Omega_+$ , of positive definite complex Hermitian matrices.

It must be noted that, for MC case, the texture is further assumed to be the same between all the real (diagonal) and

complex (off-diagonal) elements of  $\mathbf{C}$ . The MC polarimetric product model is, therefore, given by:

$$\mathbf{C} = \tau \mathbf{X} \quad (12)$$

where  $\mathbf{X}$  is a random speckle matrix. It has been shown that  $\mathbf{Y} = L\mathbf{X}$  follows a complex Wishart distribution, denoted as  $\mathbf{Y} \sim \mathcal{W}_d^{\mathbb{C}}(L, \mathbf{\Sigma})$ , where  $\mathbf{\Sigma} = \mathbf{E}\{\mathbf{X}\} = \mathbf{E}\{\mathbf{Y}\}/L$  is the speckle covariance matrix. It can be readily derived that  $\mathbf{X}$  follows a scaled complex Wishart distribution, denoted as  $\mathbf{X} \sim \mathcal{W}_d^{\mathbb{C}}(L, \mathbf{\Sigma}) |J_{\mathbf{Y} \rightarrow \mathbf{X}}|$ , where  $|J_{\mathbf{Y} \rightarrow \mathbf{X}}| = L^{d^2}$  is the Jacobian determinant of the transformation  $\mathbf{Y} = L\mathbf{X}$  [34]. The pdf of  $\mathbf{X}$  is given by:

$$p_{\mathbf{X}}(\mathbf{X}; L, \mathbf{\Sigma}) = \frac{L^{Ld} |\mathbf{X}|^{L-d}}{\Gamma_d(L) |\mathbf{\Sigma}|^L} \text{etr}(-L\mathbf{\Sigma}^{-1} \mathbf{X}) \quad (13)$$

where  $\text{etr}(\cdot)$  is the exponential of matrix trace operator, and the scaling factor,  $\Gamma_d(L)$ , is the multivariate gamma function of the complex kind, defined as:

$$\Gamma_d(L) = \pi^{d(d-1)/2} \prod_{i=0}^{d-1} \Gamma(L-i) \quad (14)$$

where  $\Gamma(\cdot)$  is a standard Euler Gamma function. If we assume that the texture remains constant within a multilook window, then the covariance matrix,  $\mathbf{\Sigma}$ , can be computed using the SCM as follows:

$$\mathbf{\Sigma}_{\text{SCM}} = \mathbf{E}\{\mathbf{C}\} = \mathbf{E}\{\tau\} \mathbf{E}\{\mathbf{X}\} = \mathbf{E}\{\tau\} \mathbf{\Sigma} \Rightarrow \mathbf{\Sigma} = \frac{\mathbf{\Sigma}_{\text{SCM}}}{\mathbf{E}\{\tau\}}, \quad (15)$$

and is normalized in the same way as it was done in (9), and (10).

## III. THE $\mathcal{G}$ DISTRIBUTION

The  $\mathcal{G}$  distribution was first proposed by Frery et al., 1997 [6] for the single-channel case, followed by its extension to MC polarimetric case by Freitas et al., 2005 [21], and recently to the SC polarimetric case by Khan et al., 2012 [25]. The product model, in conjunction with Bayes' theorem [35], can be readily used to derive closed form compound distributions assuming certain texture distributions. When the texture is modeled as GIG distributed, the return signal follows the  $\mathcal{G}$  distribution. The particular form of the  $\mathcal{G}$  distribution depends on the dimensionality of the data i.e. single-channel or polarimetric, and also on the data format i.e. singlelook or multilook.

### A. Generalized Inverse Gaussian (GIG) Texture

GIG is a very flexible univariate distribution, which has  $\gamma$ ,  $\gamma^{-1}$ , inverse gaussian, reciprocal inverse gaussian, and hyperbolic distributions as its special forms [36]. The pdf of GIG is given by [37]:

$$p_{\tau}(\tau; \alpha, \omega, \eta) = \frac{1}{\eta^{\alpha} 2 K_{\alpha}(\omega)} \tau^{\alpha-1} \exp\left(-\frac{\omega}{2} \left(\frac{\eta}{\tau} + \frac{\tau}{\eta}\right)\right), \quad (16)$$

where  $\tau > 0, \omega, \eta > 0, \alpha \in \mathbb{R}$ , and  $K_{\nu}(\cdot)$  is the modified Bessel function of the second kind and order  $\nu$ . Denoted as  $\mathcal{N}^{-1}(\alpha, \omega, \eta)$ , GIG has two shape parameters  $\alpha, \omega$ , while  $\eta$  is the scale parameter<sup>5</sup>. The shapes of GIG densities for different

<sup>5</sup>In [25], the authors used the parameterization  $\omega' = \omega/2$ ,  $\lambda' = \omega'/\eta$ ,  $\gamma' = \omega'\eta$ , where  $\prime$  denotes the parameters in [25]

values of  $\alpha$  and  $\omega$  can be found in [21]. The  $v$ -th order moments are given by:

$$\mathbf{E}\{\tau^v\} = \eta^v \frac{K_{\alpha+v}(\omega)}{K_{\alpha}(\omega)}. \quad (17)$$

GIG reduces to inverse gaussian or reciprocal inverse gaussian when  $\alpha = -\frac{1}{2}$  or  $\frac{1}{2}$ , respectively. The  $\gamma$  and  $\gamma^{-1}$  forms can be obtained by assuming  $\omega \rightarrow 0^+$  and  $\alpha$  positive or negative, respectively. While,  $\alpha = 0$  produces the hyperbolic distribution [36]. Consequently, the compound distributions of  $\mathcal{G}^h$  [26]–[28],  $\mathcal{G}^0$  and  $\mathcal{K}$  [6], [21], [25] corresponding to inverse gaussian,  $\gamma^{-1}$ , and  $\gamma$  textures, respectively, are only special forms of the  $\mathcal{G}$  distribution.

### B. Single-channel Intensity $\mathcal{G}$ Distribution

The multilook intensity  $\mathcal{G}$  distribution, denoted as  $\mathcal{G}_I(L, \alpha, \omega, \eta)$ , can be easily obtained by using (16), (2), and (3) in the product model of (1) and invoking Bayes' theorem [6]:

$$p_I(I; L, \alpha, \omega, \eta) = \frac{L^L I^{L-1}}{\Gamma(L) \eta^\alpha K_{\alpha}(\omega)} \left( \frac{2LI + \omega\eta}{\omega/\eta} \right)^{\frac{\alpha-L}{2}} \times K_{\alpha-L} \left( \sqrt{\omega/\eta (2LI + \omega\eta)} \right). \quad (18)$$

The  $v$ -th moments of  $\mathcal{G}_I$  are given by [6]:

$$\mathbf{E}\{I^v\} = \eta^v \frac{K_{\alpha+v}(\omega)}{K_{\alpha}(\omega)} \frac{\Gamma(L+v)}{L^v \Gamma(L)}. \quad (19)$$

Assuming an estimate of the shape parameters  $\alpha, \omega$  is available, the scale parameter,  $\eta$ , can be easily computed using the first moment of  $\mathcal{G}_I$  as:

$$\eta = \mathbf{E}\{I\} \frac{K_{\alpha}(\omega)}{K_{\alpha+1}(\omega)}. \quad (20)$$

### C. Singlelook Complex polarimetric $\mathcal{G}$ Distribution

The SC polarimetric  $\mathcal{G}$  distribution, denoted as  $\mathcal{G}_d(\Sigma, \alpha, \omega, \eta)$ , can be obtained by using (16), (7), and (9) in the product model of (6), and invoking Bayes' theorem [25]:

$$p_{\mathbf{C}}(\mathbf{C}; \Sigma, \alpha, \omega, \eta) = \frac{1}{\pi^d \eta^\alpha K_{\alpha}(\omega)} \left( \frac{2\mathbf{k}^H \Sigma^{-1} \mathbf{k} + \omega\eta}{\omega/\eta} \right)^{\frac{\alpha-d}{2}} \times K_{\alpha-d} \left( \sqrt{\omega/\eta (2\mathbf{k}^H \Sigma^{-1} \mathbf{k} + \omega\eta)} \right), \quad (21)$$

where  $\Sigma$  is computed and normalized using (8)–(10), as mentioned before. Assuming an estimate of the shape parameters  $\alpha, \omega$  is available, the scale parameter,  $\eta$ , can be easily computed using the first moment of GIG pdf (17), and the scale matrix normalization implication in (10), as:

$$\eta = |\Sigma_{\text{SCM}}|^{\frac{1}{d}} \frac{K_{\alpha}(\omega)}{K_{\alpha+1}(\omega)}. \quad (22)$$

### D. Multilook Complex polarimetric $\mathcal{G}$ Distribution

In a similar manner, the MC polarimetric  $\mathcal{G}$  distribution, denoted as  $\mathcal{G}_d(L, \Sigma, \alpha, \omega, \eta)$ , can be obtained by using (16), (13), and (9) in (12), and invoking Bayes' theorem [21]:

$$p_{\mathbf{C}}(\mathbf{C}; L, \Sigma, \alpha, \omega, \eta) = \frac{L^{Ld} |\mathbf{C}|^{L-d}}{\Gamma_d(L) \eta^\alpha K_{\alpha}(\omega)} \left( \frac{2L \text{Tr}(\Sigma^{-1} \mathbf{C}) + \omega\eta}{\omega/\eta} \right)^{\frac{\alpha-Ld}{2}} \times K_{\alpha-Ld} \left( \sqrt{\omega/\eta (2L \text{Tr}(\Sigma^{-1} \mathbf{C}) + \omega\eta)} \right), \quad (23)$$

where  $\Sigma$  is computed using (15), and normalized using (9), (10), as mentioned before. Again, assuming an estimate of the shape parameters  $\alpha, \omega$  is available, the scale parameter,  $\eta$ , can be easily computed using (22).

### E. Known Parameter Estimators

The parameters of  $\mathcal{G}$  distribution are inherited from the GIG texture pdf ( $\alpha, \omega, \eta$ ) and the specific speckle pdf: only  $L$  in the case of single-channel intensity, only  $\Sigma$  in the SC polarimetric case, and both ( $L, \Sigma$ ) in the matrix-variate MC polarimetric case. We start with the speckle pdf parameters, and assume that an estimate of the equivalent number of looks,  $\hat{L}$ , is given. In Section V, an estimator for  $L$ , based on log cumulants, is mentioned for both single-channel and MC polarimetric data. Computation of the normalized covariance matrix,  $\Sigma$ , based on SCM, for the SC and MC polarimetric cases, has already been given in sections III-C and III-D, respectively.

For a textureless area,  $\Sigma$  computed using SCM is known to be Maximum Likelihood (ML), unbiased, complex Wishart distributed [38], and is an example of MC polarimetric data. However, for textured areas it is neither ML nor complex Wishart distributed. In section V, we will see that the MoMLC estimation for MC polarimetric data is independent of  $\Sigma$ . However, the MoLC for SC polarimetric data is based on the Polarimetric Whitening Filter (PWF) and is, therefore, dependent on  $\Sigma$  [30]. In this case, we will estimate  $\Sigma$  using the so called Fixed Point (FP) estimator [39], denoted as  $\hat{\Sigma}_{\text{FP}}$ , listed in (50), and presented later in section V-B. Further, in the computation of  $\eta$  in (22),  $\hat{\Sigma}_{\text{FP}}$  will replace  $\Sigma_{\text{SCM}}$ . This implies, that  $\hat{\Sigma}_{\text{FP}}$  will be normalized by forcing its determinant to unity in the same way as done before, resulting in  $\tilde{\Sigma}_{\text{FP}}$ , usable in (21) in place of  $\Sigma$ . For now, we assume the SCM based  $\Sigma$ .

The scale parameter,  $\eta$ , is a nuisance parameter as it does not add any texture information, but must still be computed for analysis. Its computation for single-channel, SC, and MC polarimetric cases has already been shown in sections III-B to III-D, respectively. Two estimation techniques for the texture shape parameters  $\alpha, \omega$  of the  $\mathcal{G}$  distribution can be noted from literature. In the following, we elaborate each estimation technique:

1) *Mono-pol Fractional Moments*: This estimator is based on combining the first moment and fractional moments of the mono-pol intensity<sup>6</sup>. It is a simple extension to the estimators proposed for  $\mathcal{G}_I^0$  and  $\mathcal{K}_I$  distributions by Frery and Freitas

<sup>6</sup>No reference listing this estimator has been found in literature.

et al. [6], [40]. The first, quarter, and half moments (19) of mono-pol intensity can be combined into two equations:

$$\begin{aligned} \frac{K_{\hat{\alpha}_F + \frac{1}{4}}^2(\hat{\omega}_F)}{K_{\hat{\alpha}_F}(\hat{\omega}_F)K_{\hat{\alpha}_F + \frac{1}{2}}(\hat{\omega}_F)} \frac{\Gamma^2(L + \frac{1}{4})}{\Gamma(L)\Gamma(L + \frac{1}{2})} - \frac{\langle I^{\frac{1}{4}} \rangle^2}{\langle I^{\frac{1}{2}} \rangle} &= 0, \\ \frac{K_{\hat{\alpha}_F + \frac{1}{2}}^2(\hat{\omega}_F)}{K_{\hat{\alpha}_F}(\hat{\omega}_F)K_{\hat{\alpha}_F + 1}(\hat{\omega}_F)} \frac{\Gamma^2(L + \frac{1}{2})}{\Gamma(L)\Gamma(L + 1)} - \frac{\langle I^{\frac{1}{2}} \rangle^2}{\langle I \rangle} &= 0, \end{aligned} \quad (24)$$

which can be solved for  $\hat{\alpha}_F$ , and  $\hat{\omega}_F$ . This estimation is done on each mono-pol intensity channel. The polarimetric estimate is computed as an average of the mono-pol estimates.

2) *Numerical Maximum Likelihood Estimation*: This estimator is based on numerically maximizing the log likelihood function of the SC and MC polarimetric  $\mathcal{G}$  distributions. It was originally implemented by the authors (Khan et al. [25]) for the SC polarimetric case. Here, it has also been extended to the MC polarimetric case<sup>7</sup>. This is the only truly polarimetric estimator available in literature for the  $\mathcal{G}$  distribution. However, it is computationally very expensive as it is directly dependent on the sample size.

Given a sample of target scattering vectors,  $\mathbf{S} = \{\mathbf{k}_1, \mathbf{k}_2, \dots, \mathbf{k}_N\}$ , the log likelihood function of the SC polarimetric  $\mathcal{G}$  distribution is given by:

$$\begin{aligned} \ell(\hat{\alpha}_K, \hat{\omega}_K, \hat{\eta}_K | \mathbf{S}, \Sigma) &= N \left[ -\hat{\alpha}_K \ln(\hat{\eta}_K) - \ln\{K_{\hat{\alpha}_K}(\hat{\omega}_K)\} \right] \\ &+ \sum_{i=1}^N \left[ \left( \frac{\hat{\alpha}_K - d}{2} \right) \left[ \ln(2\mathbf{k}_i^H \Sigma^{-1} \mathbf{k}_i + \hat{\omega}_K \hat{\eta}_K) - \ln\left(\frac{\hat{\omega}_K}{\hat{\eta}_K}\right) \right] \right. \\ &\left. + \ln \left[ K_{\hat{\alpha}_K - d} \left( \sqrt{\frac{\hat{\omega}_K}{\hat{\eta}_K}} (2\mathbf{k}_i^H \Sigma^{-1} \mathbf{k}_i + \hat{\omega}_K \hat{\eta}_K) \right) \right] \right]. \end{aligned} \quad (25)$$

Similarly, given a sample of polarimetric covariance matrices,  $\mathbf{S} = \{\mathbf{C}_1, \mathbf{C}_2, \dots, \mathbf{C}_N\}$ , the log likelihood function of the MC polarimetric  $\mathcal{G}$  distribution is given by:

$$\begin{aligned} \ell(\hat{\alpha}_K, \hat{\omega}_K, \hat{\eta}_K | \mathbf{S}, L, \Sigma) &= N \left[ -\hat{\alpha}_K \ln(\hat{\eta}_K) - \ln\{K_{\hat{\alpha}_K}(\hat{\omega}_K)\} \right] \\ &+ \sum_{i=1}^N \left[ \left( \frac{\hat{\alpha}_K - Ld}{2} \right) \left[ \ln(2L \text{Tr}(\Sigma^{-1} \mathbf{C}_i) + \hat{\omega}_K \hat{\eta}_K) - \ln\left(\frac{\hat{\omega}_K}{\hat{\eta}_K}\right) \right] \right. \\ &\left. + \ln \left[ K_{\hat{\alpha}_K - Ld} \left( \sqrt{\frac{\hat{\omega}_K}{\hat{\eta}_K}} (2L \text{Tr}(\Sigma^{-1} \mathbf{C}_i) + \hat{\omega}_K \hat{\eta}_K) \right) \right] \right]. \end{aligned} \quad (26)$$

The negative of the log likelihood functions in (25) and (26) can be minimized for  $\hat{\alpha}_K$ ,  $\hat{\omega}_K$ . At each iteration of minimizer, the scale parameter  $\hat{\eta}_K$  is computed as mentioned before. The minimization algorithm used is the Nelder-Mead simplex, see [25] for more details.

<sup>7</sup>Some alternative and improved MLE techniques have also been developed for the special case of  $\mathcal{G}_I^0$  intensity distribution by Frery et al. in [41]–[43], but have not yet been extended to the  $\mathcal{G}_I$  intensity or the polarimetric  $\mathcal{G}$  distribution.

#### IV. MELLIN KIND STATISTICS: A BRIEF REVIEW

An ingenious way of dealing with radar data is to perform the statistical analysis in logarithmic domain. This elegantly separates the statistics of the radar return into an additive composition of its constituent speckle and texture parts. It was Jean-Marie Nicolas who formalised this idea into a systematic theory on logarithmic statistics for characterisation of single-channel radar data distributions, and their parameter estimation [15], [16]. This is achieved by the application of a less well known univariate Mellin transform (MT) to the pdf as opposed to the use of Fourier transform (FT) in classical statistics. Originally, referred to as *second kind statistics* by Nicolas, the framework is now increasingly being termed as *Mellin kind statistics* (MKS).

In classical statistics, the well known FT is applied to a pdf to obtain the characteristic function (CF) [35]. The  $v$ -th order derivative of the CF with respect to the transform variable gives the  $v$ -th order moment of the pdf. The logarithm of the CF, in turn, defines the cumulant generating function (CGF). The  $v$ -th order derivatives of the CF and CGF with respect to the transform variable give the  $v$ -th order (linear) moments and cumulants of the pdf, respectively.

In MKS, on the other hand, the MT is used in place of FT. Consequently, the CF and CGF are called the Mellin kind CF and CGF, respectively. The corresponding  $v$ -th order derivatives of the Mellin kind CF and CGF result in Mellin kind moments and cumulants, also referred to as log moments (LM) and log cumulants (LC), respectively.

Nicolas' MKS theory was intended for single-channel intensity/amplitude returns, defined on  $\mathbb{R}^+$ . It was the work of Anfinson et al. [29], that extended the MKS theory to MC polarimetric matrix-variate data by using the matrix-variate MT. Later, Anfinson also developed asymptotic MKS for SC polarimetric case by applying Nicolas' univariate MKS to singlelook polarimetric whitening filter (PWF) [30], [44]. In the following, we briefly list the MKS relevant to this contribution:

##### A. Mellin Transform

The MT of a real valued function  $f(x)$  defined on  $\mathbb{R}^+$  is:

$$F(s) = \mathcal{M}\{f(x)\}(s) = \int_0^\infty x^{s-1} f(x) dx \quad (27)$$

where  $s \in \mathbb{C}$  is a complex transform variable, but, under certain conditions  $s \in \mathbb{R}$  [29].

The MT of a real valued scalar function  $f(\mathbf{X})$  defined on a cone  $\Omega_+$  of complex, positive definite and Hermitian matrices with dimension  $d \times d$  is [29]:

$$F(s) = \mathcal{M}\{f(\mathbf{X})\}(s) = \int_{\Omega_+} |\mathbf{X}|^{s-d} f(\mathbf{X}) d\mathbf{X} \quad (28)$$

where it is also assumed that  $f(\mathbf{XY}) = f(\mathbf{YX})$  for  $\mathbf{X}, \mathbf{Y} \in \Omega_+$ .

### B. Univariate Mellin Kind Statistics

The univariate MT (27) is directly applicable on amplitude and intensity pdfs because of the common domain. Hence, the Mellin kind CF of pdf,  $p_I(I)$ , is given by:

$$\begin{aligned}\phi_I(s) &= \mathbf{E}\{I^{s-1}\} = \mathcal{M}\{p_I(I)\}(s) \\ &= \int_0^\infty e^{(s-1)\ln I} p_I(I) dI \\ &= \sum_{v=0}^\infty \frac{(s-1)^v}{v!} \int_0^\infty (\ln I)^v p_I(I) dI \\ &= \sum_{v=0}^\infty \frac{(s-1)^v}{v!} \mu_v\{I\}\end{aligned}\quad (29)$$

where the exponential function has been expanded in Maclaurin series. This shows that the Mellin kind CF of  $p_I(I)$  can be expanded in terms of its log moments (LM),  $\mu_v\{I\} = \mathbf{E}\{(\ln I)^v\}$ . The LMs can be retrieved from  $\phi_I(s)$  as:

$$\mu_v\{I\} = \left. \frac{d^v}{ds^v} \phi_I(s) \right|_{s=1} \quad (30)$$

Similarly, the Mellin kind CGF, given by  $\varphi_I(s) = \ln\{\phi_I(s)\}$ , can also be expanded as:

$$\varphi_I(s) = \sum_{v=0}^\infty \frac{(s-1)^v}{v!} \kappa_v\{I\} \quad (31)$$

where  $\kappa_v\{I\}$  are the log cumulants (LC), which can be retrieved from  $\varphi_I(s)$  as:

$$\kappa_v\{I\} = \left. \frac{d^v}{ds^v} \varphi_I(s) \right|_{s=1} \quad (32)$$

### C. Matrix-variate Mellin Kind Statistics

The matrix-variate MT (28) is applicable to multilook polarimetric covariance matrix pdfs because of the common domain. In this case, the Mellin kind CF is given by:

$$\begin{aligned}\phi_{\mathbf{C}}(s) &= \mathbf{E}\{|\mathbf{C}|^{s-d}\} = \mathcal{M}\{p_{\mathbf{C}}(\mathbf{C})\}(s) \\ &= \sum_{v=0}^\infty \frac{(s-d)^v}{v!} \mu_v\{\mathbf{C}\}\end{aligned}\quad (33)$$

which shows that the Mellin kind CF of  $p_{\mathbf{C}}(\mathbf{C})$  can also be expanded in terms of matrix log moments (MLM), given by  $\mu_v\{\mathbf{C}\} = \mathbf{E}\{(\ln |\mathbf{C}|)^v\}$ . The MLMs can be retrieved from  $\phi_{\mathbf{C}}(s)$  as:

$$\mu_v\{\mathbf{C}\} = \left. \frac{d^v}{ds^v} \phi_{\mathbf{C}}(s) \right|_{s=d} \quad (34)$$

Similarly, the Mellin kind CGF, given by  $\varphi_{\mathbf{C}}(s) = \ln\{\phi_{\mathbf{C}}(s)\}$ , can also be expanded as:

$$\varphi_{\mathbf{C}}(s) = \sum_{v=0}^\infty \frac{(s-d)^v}{v!} \kappa_v\{\mathbf{C}\} \quad (35)$$

where  $\kappa_v\{\mathbf{C}\}$  are the matrix log cumulants (MLC), which can be retrieved from  $\varphi_{\mathbf{C}}(s)$  as:

$$\kappa_v\{\mathbf{C}\} = \left. \frac{d^v}{ds^v} \varphi_{\mathbf{C}}(s) \right|_{s=d} \quad (36)$$

### D. Relations between Moments and Cumulants

The moments and cumulants of a pdf are directly related to each other. The cumulants can be computed as a polynomial of moments up to the same order and vice versa. This is irrespective of the fact that they are log or linear and also independent of the type of random variate. Relations upto the tenth order are listed in [45], and the first three are given here:

$$\kappa_1 = \mu_1 \quad (37)$$

$$\kappa_2 = \mu_2 - \mu_1^2 \quad (38)$$

$$\kappa_3 = \mu_3 - 3\mu_1\mu_2 + 2\mu_1^3 \quad (39)$$

It should be noted that the first LC is dependent on scale parameter. The second and higher order LCs, if they exist, are independent of scale and can be used for the estimation of shape parameters of the pdf. Also, the sample LCs can be obtained by first computing sample LMs up to the same order and then using the equations above.

### E. Product Model Mellin Kind Statistics

In the realm of compound pdfs defined by the product model, MKS framework plays a significant role in statistical analysis. The MT has certain advantages in its application to the product model. This behaviour has a direct analogy in the application of FT, due to its convolution property, to additive noise signal model. Nicolas, in [15], showed that for the univariate product model in (1), the following relations hold:

$$p_I(I) = p_\tau(\tau) \hat{\star} p_x(x) \quad (40)$$

$$\phi_I(s) = \phi_\tau(s) \cdot \phi_x(s) \quad (41)$$

$$\varphi_I(s) = \varphi_\tau(s) + \varphi_x(s) \quad (42)$$

$$\kappa_v\{I\} = \kappa_v\{\tau\} + \kappa_v\{x\} \quad (43)$$

where  $\hat{\star}$  denotes the Mellin kind convolution. Equation (41) follows directly from (40) and the convolution property of MT:

$$\mathcal{M}\{p_\tau(\tau) \hat{\star} p_x(x)\}(s) = \mathcal{M}\{p_\tau(\tau)\}(s) \cdot \mathcal{M}\{p_x(x)\}(s) \quad (44)$$

Equation (43) shows that the LCs of intensity return decompose as the sum of LCs of texture and speckle random variables.

Anfinsen et al. [29] derived equivalent relations for the polarimetric covariance matrix product model (12):

$$\phi_{\mathbf{C}}(s) = \phi_\tau(d(s-d)+1) \cdot \phi_{\mathbf{X}}(s) \quad (45)$$

$$\varphi_{\mathbf{C}}(s) = \varphi_\tau(d(s-d)+1) + \varphi_{\mathbf{X}}(s) \quad (46)$$

$$\kappa_v\{\mathbf{C}\} = d^v \kappa_v\{\tau\} + \kappa_v\{\mathbf{X}\} \quad (47)$$

Equation (47) shows that the observed MLCs decompose as a sum of speckle MLCs and texture LCs scaled by  $d^v$ .

## V. METHOD OF LOG CUMULANT ESTIMATION

In classical statistics, the well known method of moments (MoM) is employed to estimate the parameters of a pdf. This is based on solving as many moment equations as the number of unknown parameters and substituting population moments with sample moments. The estimates can generally be improved by using more moment equations than the number of

unknown parameters in the form of an optimization problem. The covariance matrix of the sample moments is used as a weighting matrix in the optimization. This is also referred to as the generalized method of moments (GMoM) [46].

In MKS, direct counterparts of MoM and GMoM exist and are called MoLC [15], [30] and Generalized MoLC (GMoLC), respectively. The only difference being that, in place of moment equations, LC equations are used, sample LCs substitute population LCs. Further, in GMoLC, the covariance matrix of sample LCs, instead of sample moments, is used as a weighting matrix. For the matrix-variate case, these methods are intuitively called method of matrix log cumulants (MoMLC) [29] and generalized MoMLC (GMoMLC) [31].

In practice, the LC (43) and MLC (47) relations, derived using the product model MKS, can be used in the MoLC and MoMLC estimation, respectively. This results in estimators with good statistical properties like low bias and variance [29]. It must be noted that the mathematical expressions of texture LCs,  $\kappa_v\{\tau\}$ , depend on the choice of the texture pdf. The LCs of speckle are generally quite well defined under certain assumptions (see Section I). Extensive account on this can be found in [15], [24], [29], [30].

The LCs of GIG texture pdf will be defined in Section VI. In the following we list the speckle LCs for the intensity, SC polarimetric scattering vector, and MC polarimetric covariance matrix cases of the product model.

#### A. Intensity Case

Multilook intensity speckle is  $\gamma$  distributed (2) and its LCs are given by [15]:

$$\kappa_v\left\{x; \frac{\sigma^2}{L}, L\right\} = \begin{cases} \psi^{(0)}(L) + \ln\left(\frac{\sigma^2}{L}\right) & \text{for } v = 1, \\ \psi^{(v-1)}(L) & \text{for } v > 1. \end{cases} \quad (48)$$

where  $\psi^{(v)}(\cdot)$  is the  $v$ -th order polygamma function. Interestingly, over a textureless area, the first order LC equation can be easily used to estimate  $\hat{L}$ . This is done by first computing the mean intensity,  $\sigma^2$ , followed by numerically solving the first order LC equation for  $\hat{L}$ , after substituting sample LCs,  $\langle\kappa_1\{x\}\rangle$ , in place of theoretical LCs,  $\kappa_1\{x\}$ . Alternatively, the second order LC equation, alone, can also be used in a similar way as shown by Nicolas in [15].

#### B. Singlelook Complex Polarimetric Scattering Vector Case

Speckle LCs for SC polarimetric data have only been derived for the asymptotic case. The derivation is not as straight forward as for the intensity or MC polarimetric case. Here, we will only list the most relevant analysis and results. Detailed explanation can be found in the work of Anfinen [30].

Let us examine the product model decomposition of the fixed-point polarimetric whitening filter (FP-PWF):

$$y = \mathbf{k}^H \hat{\Sigma}_{\text{FP}}^{-1} \mathbf{k} = \tau(\mathbf{x}^H \hat{\Sigma}_{\text{FP}}^{-1} \mathbf{x}) = \tau Q, \quad (49)$$

where the quadratic form  $Q$  represents the speckle contribution, and  $\hat{\Sigma}_{\text{FP}}$  is the FP estimator of  $\Sigma$  given by [39]:

$$\hat{\Sigma}_{\text{FP}} = \frac{d}{N} \sum_{i=1}^N \frac{\mathbf{k}_i \mathbf{k}_i^H}{\mathbf{k}_i^H \hat{\Sigma}_{\text{FP}}^{-1} \mathbf{k}_i}, \quad (50)$$

where  $N$  is the sample size. Anfinen [30] found that  $Q$  asymptotically follows a Fisher variate,  $\mathcal{F}(m, a, b)$ , with parameterization given in [15]:

$$Q \stackrel{N \rightarrow \infty}{\sim} \frac{Nd}{N-d+(1/d)} \mathcal{F}_{1,d,(\frac{d}{d+1})(N-d+(1/d))}, \quad (51)$$

whose LCs are given by [30]:

$$\begin{aligned} \kappa_1\{Q\} &= \psi^{(0)}(d) - \psi^{(0)}\left(\frac{d(N-d+\frac{1}{d})}{d+1}\right) \\ &\quad + \ln\left(\frac{Nd}{(d+1)} \frac{(N-d-1)}{(N-d+\frac{1}{d})}\right) \end{aligned} \quad (52)$$

$$\kappa_{v>1}\{Q\} = \psi^{(v-1)}(d) - \psi^{(v-1)}\left(\frac{d(N-d+\frac{1}{d})}{d+1}\right) \quad (53)$$

It is important to note that the product model decomposition in the SC polarimetric case is univariate. Therefore, the SC MoLC uses MKS of the univariate case (40)-(43).

#### C. Multilook Complex Polarimetric Covariance Matrix Case

MC polarimetric speckle follows a scaled complex Wishart distribution (13), whose LCs are given by [29]:

$$\kappa_v\{\mathbf{X}; L, \Sigma\} = \begin{cases} \psi_d^{(0)}(L) + \ln|\Sigma| - d \ln L & \text{for } v = 1, \\ \psi_d^{(v-1)}(L) & \text{for } v > 1. \end{cases} \quad (54)$$

where  $\psi_d^{(v)}(\cdot)$  is the  $v$ -th order multivariate polygamma function of the complex kind, defined as  $\psi_d^{(v)}(z) = \sum_{i=0}^{d-1} \psi^{(v)}(z-i)$ . Notice, that the first order MLC equation can be easily used to estimate  $\hat{L}$  over a textureless area as shown in [47].

### VI. GENERALIZED INVERSE GAUSSIAN MELLIN KIND STATISTICS

The univariate MKS, visited in Section IV-B, can be directly applied to the GIG texture pdf (16). In the following, we present the mathematical forms of the Mellin kind CF, CGF, and LCs of GIG pdf.

#### A. Mellin Kind Characteristic Function

The Mellin kind CF of GIG pdf can be derived by applying the univariate MT on (16):

$$\begin{aligned} \phi_\tau(s; \alpha, \omega, \eta) &= \mathcal{M}\{p_\tau(\tau; \alpha, \omega, \eta)\}(s) \\ &= \frac{1}{2\eta^\alpha K_\alpha(\omega)} \int_{\mathbb{R}_+} \tau^{\alpha+s-2} e^{(-\frac{\omega\eta}{2\tau} - \frac{\omega\tau}{2\eta})} d\tau, \end{aligned} \quad (55)$$

multiplying and dividing the right hand side of (55) by  $\eta^{s-1}$  and using the following integral relation of modified Bessel functions:

$$K_\nu(2\sqrt{ab}) = \frac{(\frac{a}{b})^{\frac{\nu}{2}}}{2} \int_{\mathbb{R}_+} u^{\nu-1} e^{(-au - \frac{b}{u})} du, \quad (56)$$

eq. (55) reduces to:

$$\phi_\tau(s; \alpha, \omega, \eta) = \eta^{s-1} \frac{K_{\alpha+s-1}(\omega)}{K_\alpha(\omega)}. \quad (57)$$

### B. Mellin Kind Cumulant Generating Function

The Mellin kind CGF of GIG pdf is thus given by:

$$\varphi_\tau(s; \alpha, \omega, \eta) = (s-1) \ln \eta + \ln K_{\alpha+s-1}(\omega) - \ln K_\alpha(\omega). \quad (58)$$

### C. Log Cumulants

The LCs of GIG pdf can be found by applying (32) on (58):

$$\kappa_v\{\tau; \alpha, \omega, \eta\} = \begin{cases} \ln \eta + \ln K_\alpha^{(1)}(\omega) & \text{for } v = 1, \\ \ln K_\alpha^{(v)}(\omega) & \text{for } v > 1. \end{cases} \quad (59)$$

where  $\ln K_\alpha^{(v)}(\omega) = \frac{d}{ds^v} \ln K_{\alpha+s-1}(\omega) \big|_{s=1}$  i.e. the  $v$ -th derivative, with respect to order, of the logarithm of modified Bessel function of the second kind. No special function exists for directly computing  $\ln K_\alpha^{(v)}(\omega)$ , therefore we must resort to numerical differentiation. For now, it is interesting to derive two special cases of GIG LCs. The advantage of this will become apparent later in this section.

The two cases correspond to the  $\gamma$  and  $\gamma^{-1}$  special forms of the GIG pdf. These special pdfs have been studied in detailed in [6], [21], [25]. Also, their LCs are well defined [15]. The first case corresponding to the  $\gamma$  pdf, arrives when  $\omega \rightarrow 0^+$  and  $\alpha + s - 1 > 0$ . Let us list the following two relations of modified Bessel functions, which will be useful:

$$K_\nu(\mu) = 2^{\nu-1} \Gamma(\nu) \mu^{-\nu}, \quad (60)$$

$$K_\nu(\mu) = K_{-\nu}(\mu). \quad (61)$$

Also, the definition of polygamma function will be useful [35]:

$$\psi^{(m)}(x) = \frac{d^{m+1}}{dx^{m+1}} \ln \Gamma(x), \quad m = 0, 1, 2, \dots \quad (62)$$

where  $m = 0$  represents the digamma function. Equation (60) only holds for positive order and small values of argument, which are exactly the assumptions in our first case. Then, using (60) and (62) in (59), one can easily derive:

$$\kappa_v\{\tau; \alpha, \omega, \eta\} \underset{\omega \rightarrow 0^+}{\overset{\alpha > 0}{\sim}} \begin{cases} \ln\left(\frac{2\eta}{\omega}\right) + \psi^{(0)}(\alpha) & \text{for } v = 1, \\ \psi^{(v-1)}(\alpha) & \text{for } v > 1. \end{cases} \quad (63)$$

Equation (63) proves that the GIG LCs are asymptotically equivalent to  $\gamma$  LCs under the given parametric assumptions. It must be pointed out that the term  $\frac{2\eta}{\omega}$  is the scale parameter of  $\gamma$  pdf.

Similarly, the second case, corresponding to the  $\gamma^{-1}$  pdf, results when  $\omega \rightarrow 0^+$  and  $\alpha + s - 1 < 0$ . In this case, (61) is first used to make the order of modified Bessel function positive. Finally, again using (60) and (62) in (59) one finds:

$$\kappa_v\{\tau; \alpha, \omega, \eta\} \underset{\omega \rightarrow 0^+}{\overset{\alpha < 0}{\sim}} \begin{cases} \ln\left(\frac{\omega\eta}{2}\right) - \psi^{(0)}(-\alpha) & \text{for } v = 1, \\ (-1)^v \psi^{(v-1)}(-\alpha) & \text{for } v > 1. \end{cases} \quad (64)$$

Equation (64) proves that the GIG LCs are also asymptotically equivalent to  $\gamma^{-1}$  LCs. Also,  $\frac{\omega\eta}{2}$  is the scale parameter of  $\gamma^{-1}$  pdf.

Let us now turn our attention back to numerical differentiation i.e. computing  $\ln K_\alpha^{(v)}(\omega)$ . We have used the well known extended Neville's algorithm to obtain derivatives numerically (see [48], [49]). This algorithm is also implemented in the commercial *Numerical Algorithms Group (NAG) Fortran library* as routine *d04aaf*, which computes derivatives of an analytical function up to the fourteenth order. However, we have used a well documented Matlab version of the same algorithm easily available at [50], [51]. This implementation only computes derivatives up to the fourth order. We have extended this to compute the first eight derivatives<sup>8</sup>. This implementation uses Taylor series expansion of a function up to a certain order around some point  $x_0$ . It then rearranges the expansion to form a finite difference approximation to compute the  $v$ -th derivative of the function at  $x_0$ . The derivative is approximated at a sequence of points following a log spacing away from  $x_0$ . The maximum point away from  $x_0$  should be the same order of magnitude as that of the shape parameters  $\alpha, \omega$  (whichever is greater). Further, the algorithm reduces the amount of work by approximating the even and odd order derivatives by only using even and odd Taylor series expansions, respectively. Finally, Romberg extrapolation is used to improve the approximations. The reader is encouraged to study the algorithm and its implementation in detail at the above mentioned references. However, we restrict ourselves here to only show the accuracy of the GIG LCs computed using this algorithm. It should be noted that  $\ln K_\alpha^{(v)}(\omega)$  can also be computed by first computing  $K_\alpha^{(v)}(\omega)$  (i.e. without the logarithm transformation) up to order  $v$ , followed by the application of the well known Leibniz product rule. This alternative has not been tested.

The accuracy of GIG LCs is validated by comparing them to the asymptotic case of  $\gamma$  LCs (63). Equivalently, (64) could have also been used for this purpose. Let us assume  $\alpha = 5$ ,  $\eta = 1$ , and  $\omega = 10^{-6}$ . Then, we can compute the first eight GIG LCs (59) and the first eight  $\gamma$  LCs (63), and compare their values to find  $\epsilon_v$ , the relative error:

$$\epsilon_v = \frac{\kappa_v^{\text{GIG}} - \kappa_v^{\text{gamma}}}{\kappa_v^{\text{gamma}}} \quad (65)$$

where the superscript is shown only to distinguish between the two LCs. Table I shows the first eight GIG and  $\gamma$  LCs, along with the absolute value of the relative error. Note that the  $\gamma$  LCs are represented in their standard two parameter form,  $\kappa_v\{\alpha, \frac{2\eta}{\omega}\}$ , and also the reference to the texture random variable,  $\tau$ , has been dropped. The relative error is reasonably low and increases for higher order LCs, as expected. For the eighth LC it is of order  $10^{-4}$ . For even smaller values of  $\omega \approx 10^{-10}$ , the error does not decrease significantly. Also, it was observed that the order of magnitude of the error approximately remains the same whatever value of  $\alpha$  is chosen. It is important to mention that only the second and third GIG LCs, with very small relative error, are used for parameter estimation. We will see later that the higher order LCs are only utilized in GoF testing, and their accuracy is acceptable for the purpose at hand.

<sup>8</sup>The Matlab implementation of this algorithm can be obtained from the corresponding author on request.



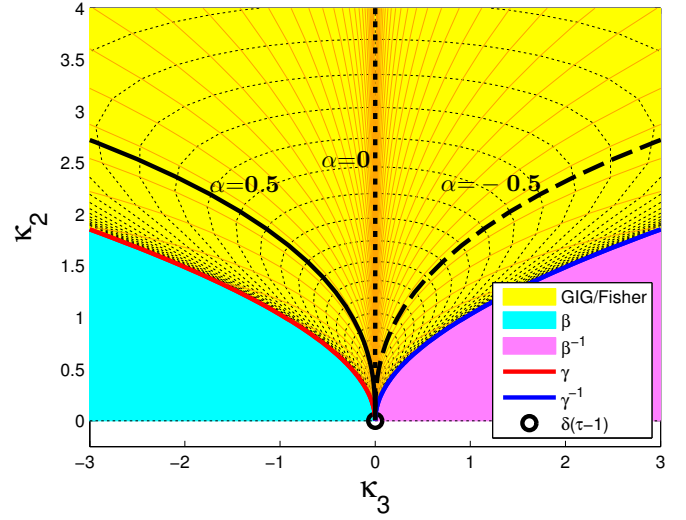
TABLE I

GIG AND GAMMA PDF LOG CUMULANTS AT  $\alpha = 5, \omega = 10^{-6}, \eta = 1$ .

	GIG LC	Gamma LC	
$v$	$\kappa_v\{\cdot; \alpha, \omega, \eta\}$	$\kappa_v\{\cdot; \alpha, \frac{2\eta}{\omega}\}$	$ \epsilon_v $
1	16.014775406956350	16.014775406956020	$2.06 \times 10^{-14}$
2	0.221322955738990	0.221322955737115	$8.47 \times 10^{-12}$
3	-0.048789732107969	-0.048789732245114	$2.81 \times 10^{-9}$
4	0.021427827882668	0.021427828192755	$1.45 \times 10^{-8}$
5	-0.014063194626264	-0.014063191342113	$2.34 \times 10^{-7}$
6	0.012261446278990	0.012261509635954	$5.17 \times 10^{-6}$
7	-0.013315057585594	-0.013316295488551	$9.30 \times 10^{-5}$
8	0.017291171522857	0.017295357774073	$2.42 \times 10^{-4}$

Let us now give a geometrical representation to the GIG LCs. In [15], Nicolas first proposed the univariate  $(\kappa_3, \kappa_2)$  LC diagram. A matrix-variate extension to this geometrical representation was presented in [29], resulting in the  $(\kappa_3\{\mathbf{C}\}, \kappa_2\{\mathbf{C}\})$  MLC diagram. We restrict our presentation to the univariate LC diagram as even the MLCs can be translated back to the univariate texture LCs after subtracting out the speckle MLCs and appropriate scaling (rearranging (47)). This diagram is based on our earlier observation that the second and higher order LCs are independent of the scale, and are only dependent on the texture shape parameters and the number of looks. Considering the number of looks as a constant throughout the SAR image, the LC diagram shows the solitary impact of texture shape parameters on the model. The LC diagram simultaneously shows 1) the manifolds spanned by the theoretical population LCs attainable under given pdf models, and 2) points that represent empirical sample LCs computed from data. The dimension of the manifold spanned by a distribution model is equal to the number of texture parameters. As a result,  $\gamma$  and  $\gamma^{-1}$  pdfs are represented by a line, while  $\beta$ ,  $\beta^{-1}$ ,  $\mathcal{F}$ , and GIG pdfs are represented by surfaces. The degenerate textureless case (Dirac delta) will thus be represented by a point. For a more general definition of the LC diagram see [29].

Figure 1 shows the manifolds spanned by the theoretical population LCs under different texture distribution models. The GIG LCs occupy the whole yellow space asymptotically reducing into the  $\gamma$  and  $\gamma^{-1}$  LCs. This also shows that the GIG pdf is very flexible in terms of the texture shapes it can attain. Interestingly, the  $\mathcal{F}$  distribution also occupies the same LC space in  $(\kappa_3, \kappa_2)$  diagram [24]. The figure also shows two sets of orange and dotted black lines within the GIG LC space. These lines represent equi- $\alpha$  and equi- $\omega$  curves, respectively. Along an equi- $\alpha$  curve (orange),  $\omega$  logarithmically increases as we move towards the textureless case, represented by the black circle. Some special equi- $\alpha$  manifolds have also been highlighted by thick black lines. These represent the inverse gaussian (long dashes), reciprocal inverse gaussian (solid), and hyperbolic (short dashes) distributions corresponding to  $\alpha = -0.5$ ,  $\alpha = 0.5$ , and  $\alpha = 0$ , respectively. The asymptotic cases of  $\gamma$  and  $\gamma^{-1}$  arise when  $\omega$  approaches zero, represented by the red and blue manifolds, respectively. Along an equi- $\omega$  curve (dotted black),  $\alpha$  approaches zero when  $\kappa_3$  tends to zero,  $\alpha$  is positive when  $\kappa_3$  is negative, and vice versa. Also, on either side along this curve  $|\alpha|$  increases logarithmically

Fig. 1. Theoretical GIG pdf log cumulants in  $(\kappa_3, \kappa_2)$  LC diagram.

towards the textureless case. It must also be pointed out that the GIG LCs are symmetric about  $\kappa_3 = 0$ .

## VII. LOG CUMULANTS OF $\mathcal{G}$ DISTRIBUTION

We are now in a position to list the LC expressions for the  $\mathcal{G}$  distribution. For the multilook intensity case we can put (59), (48), and (3) in (43):

$$\begin{aligned} \kappa_v\{I; L, \alpha, \omega, \eta\} &= \\ &= \begin{cases} \ln\left(\frac{\eta}{L}\right) + \psi^{(0)}(L) + \ln K_{\alpha}^{(1)}(\omega) & \text{for } v = 1, \\ \psi^{(v-1)}(L) + \ln K_{\alpha}^{(v)}(\omega) & \text{for } v > 1. \end{cases} \end{aligned} \quad (66)$$

Assuming we have an estimate of  $\hat{L}$ , we can estimate mono-pol  $\hat{\alpha}_N, \hat{\omega}_N^9$  by simultaneously solving second and third order LC equations after replacing population LCs with sample LCs. The mono-pol estimates can be averaged to obtain estimates for the polarimetric pdf.

In the SC polarimetric case we can combine (59), (52), and (53) by applying univariate MKS (43) on product model decomposition of FP-PWF:

$$\begin{aligned} \kappa_1\{y; \alpha, \omega, \eta\} &= \psi^{(0)}(d) - \psi^{(0)}\left(\frac{d(N-d+\frac{1}{d})}{d+1}\right) \\ &+ \ln\left(\frac{\eta Nd}{(d+1)(N-d+\frac{1}{d})}\right) + \ln K_{\alpha}^{(1)}(\omega) \\ \kappa_{v>1}\{y; \alpha, \omega\} &= \psi^{(v-1)}(d) + \ln K_{\alpha}^{(v)}(\omega) \\ &- \psi^{(v-1)}\left(\frac{d(N-d+\frac{1}{d})}{d+1}\right) \end{aligned} \quad (67)$$

$$(68)$$

again we can estimate  $\hat{\alpha}_{A1}, \hat{\omega}_{A1}^9$  by simultaneously solving second and third order LC equations after replacing population LCs with sample LCs.

<sup>9</sup>The subscript is used to keep nomenclature consistency with Anfin's contribution [29]. 'N' for Nicolas mono-pol estimators, 'A1' for Anfin's MoLC and MoMLC based estimators, 'F' for Frery's mono-pol estimators (24), and 'K' for Khan's numerical MLE based polarimetric estimators (25), and (26).

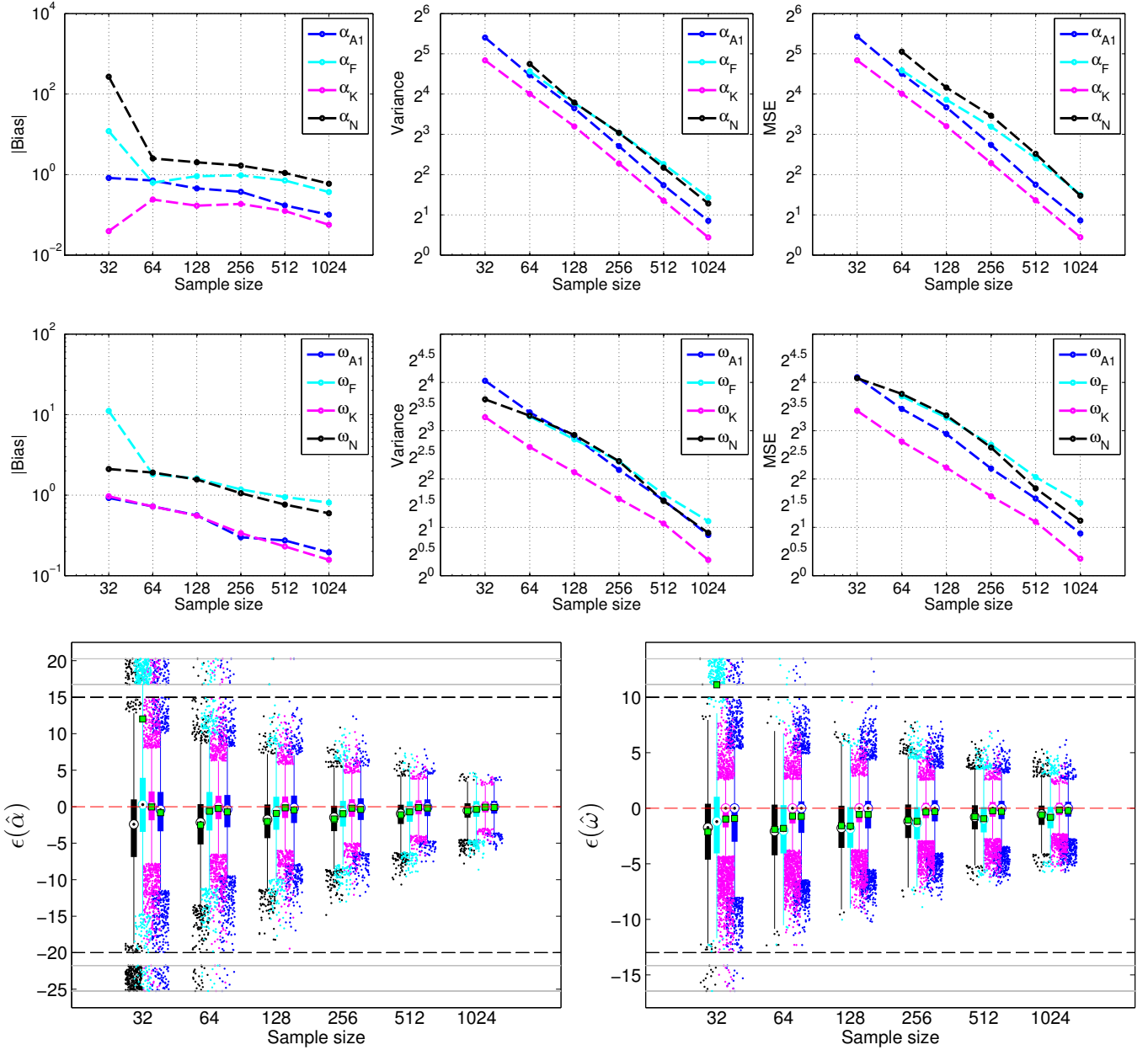


Fig. 2. Estimator performance analysis for MC polarimetric  $\mathcal{G}$  distribution texture shape parameters  $\alpha$ , and  $\omega$  after 5030 Monte Carlo simulations. True value:  $\alpha=5$ ,  $\omega=5$  at  $L=10$ . (Top row) Estimator bias (left), variance (middle), and MSE (right) for  $\alpha$ , and (Middle row) the same for  $\omega$  as functions of sample size. (Bottom row) Box plots of estimator error,  $\epsilon(\cdot)$ , for (left)  $\alpha$ , and (right)  $\omega$ . The tiny black dots and green squares represent the medians and means, respectively. The mean estimator error is the bias. Outliers are larger than  $q_3 + w(q_3 - q_1)$  or smaller than  $q_1 - w(q_3 - q_1)$ , where  $q_1$ ,  $q_2$ , and  $q_3$  are the median, 25<sup>th</sup>, and 75<sup>th</sup> percentiles, respectively, while  $w=1.5$  is the whisker length corresponding to  $\pm 2.7$  standard deviation for gaussian data. Data points above and below black dashed lines are compressed inside gray lines for plot legibility. Red dashed lines indicate zero error.

For MC polarimetric case we can combine (59), (54), and (9) in (47):

$$\begin{aligned} \kappa_v\{\mathbf{C}; L, \alpha, \omega, \eta\} &= \\ &= \begin{cases} d \ln\left(\frac{\eta}{L}\right) + \psi_d^{(0)}(L) + d \ln K_\alpha^{(1)}(\omega) & \text{for } v = 1, \\ \psi_d^{(v-1)}(L) + d^v \ln K_\alpha^{(v)}(\omega) & \text{for } v > 1. \end{cases} \end{aligned} \quad (69)$$

Similar to the previous cases, we can estimate  $\hat{\alpha}_{A1}, \hat{\omega}_{A1}$ <sup>9</sup> by simultaneously solving second and third order LC equations after replacing population MLCs with sample MLCs, and

assuming  $\hat{L}$  is given.

One critical observation must be made. If the sample LCs fall outside the GIG manifold in  $(\kappa_3, \kappa_2)$  LC diagram, then only  $\alpha$  needs to be estimated as  $\omega$  is close to zero. The GIG LCs (59) reduce to  $\gamma$  (63) or  $\gamma^{-1}$  (64) LCs depending on the sign of  $\kappa_3$ . Consequently, the  $\mathcal{G}$  LCs reduce to  $\mathcal{K}$  or  $\mathcal{G}^0$  LCs, respectively.

## VIII. ESTIMATOR PERFORMANCE ANALYSIS

We have performed Monte Carlo simulations to compare the performance of different estimators for texture parameters

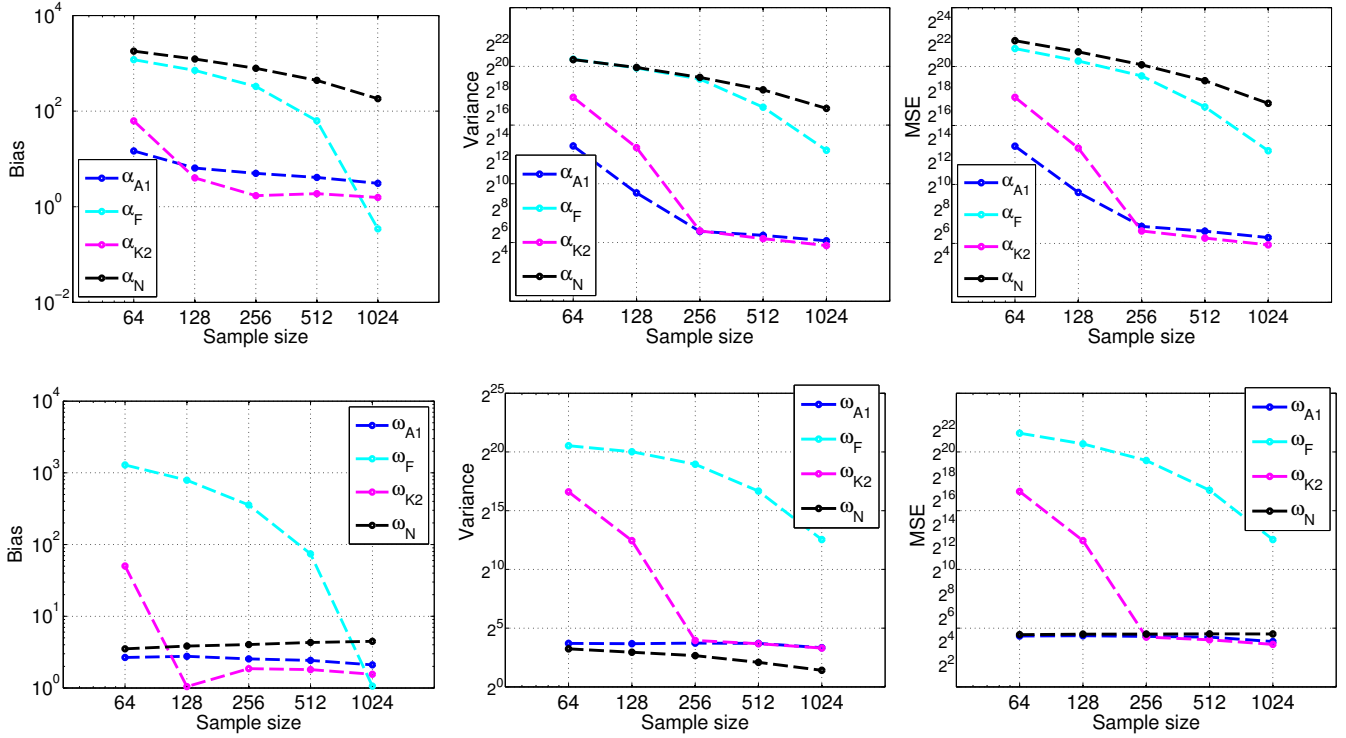


Fig. 3. Estimator performance analysis for SC polarimetric  $\mathcal{G}$  distribution texture shape parameters  $\alpha$ , and  $\omega$ . Estimator bias (left), variance (middle), and MSE (right) for  $\alpha$  (top row), and for  $\omega$  (bottom row) as a function of sample size. True value:  $\alpha=5$ ,  $\omega=5$  at  $L=1$ .

TABLE II  
COMPUTATION TIME (MILLISECONDS) OF ESTIMATION ON SIMULATED  
MC POLARIMETRIC DATA WITH SAMPLE SIZE 256.

	Mean	Max.
$\mathcal{G}_{A1}$	56.4	192.3
$\mathcal{G}_K$	25.2	162.1
$\mathcal{G}_F$	91.3	319.5
$\mathcal{G}_N$	208.9	679.2

of polarimetric  $\mathcal{G}$  distribution. This has been carried out for both simulated SC and MC polarimetric SAR data. In each of the two cases we have compared four estimators, namely 1) Nicolas' mono-pol estimator (N estimator) i.e.  $\hat{\alpha}_N, \hat{\omega}_N$  using (66) for both SC and MC polarimetric data, 2) Anfinson's estimator (A1 estimator) i.e.  $\hat{\alpha}_{A1}, \hat{\omega}_{A1}$  using (68) and (69) for SC and MC polarimetric data, respectively, 3) Frery's mono-pol estimator (F estimator) i.e.  $\hat{\alpha}_F, \hat{\omega}_F$  using (24) for both SC and MC polarimetric data, and 4) Khan's numerical maximum likelihood estimator (K estimator) i.e.  $\hat{\alpha}_K, \hat{\omega}_K$  using (25), and (26) for SC and MC polarimetric data, respectively. For N and A1 estimators, only second and third order equations are used for estimation as explained in section VII.

Figure 2 shows the bias, variance, mean squared error (MSE), and box plots of estimator error for the four estimators after 5030 Monte Carlo simulations with  $\alpha=5$ ,  $\omega=5$ , and  $L=10$  at different sample sizes. The plots of bias, variance, and MSE are simply a summary of the detailed estimator errors represented in the form of box plots in the bottom row of fig. 2. In fact, the summary results can be easily validated by comparisons with the corresponding box plots as

the same color coding has been used. Clearly, the polarimetric estimators show lower bias than the mono-pol estimators. The bias, variance, and MSE of the K estimator is generally the lowest. The variances of F and N estimators of  $\alpha$  are too high for sample size 32, and hence omitted. The same is also true for F estimator of  $\omega$  at sample size 32. The variance of A1 estimator of  $\alpha$  is clearly lower than those of F and N estimators, while the variances of the F, N and A1 estimators of  $\omega$  are very similar. However, even with similar variances for  $\omega$ , the performance of F and N estimators is degraded by the higher bias. This is highlighted by computing MSE, which is a sum of the variance and squared bias. The lower MSE of A1 estimator than F and N estimators for both shape parameters is evident for all sample sizes. Therefore, we can conclude that the two polarimetric estimators perform better than the mono-pol estimators. Between the polarimetric estimators, K estimator performs better. However, this is tainted by the fact, that for large samples, it is computationally extremely expensive as it is directly dependent on the sample size. The computation times of the four estimators were also recorded in the Monte Carlo simulations using Matlab software on a 3.10 gigahertz processor with 8 gigabytes of memory. Their mean and maximum values at sample size of 256 are shown in table II, which shows that the computational time of A1 estimator competes well with other estimators. Interestingly, the K estimator is faster at this sample size, but it will become slower as the sample size increases. Finally, between the two mono-pol estimators, the F estimator exhibits lower bias, similar variance, and lower MSE for  $\alpha$ , but for  $\omega$  the performance is generally very similar except for samples size

greater than 256, where the N estimator shows lower bias, variance, and MSE. We have observed very similar bias, variance, and MSE at other values of  $\alpha$ ,  $\omega$ , and  $L$  as well.

Figure 3 shows exactly the same scenario but for simulated SC polarimetric data. The box plots have been omitted for brevity. It should be mentioned here that, although A1 estimator has been derived using asymptotic statistics, we boldly apply it on finite samples. The results clearly show that both the polarimetric estimators perform significantly better than the mono-pol estimators. Between the polarimetric estimators, although A1 has a slightly higher bias than K for sample size greater than 100, it has a significantly better variance for sample size smaller than 256. This reflects as significantly better MSE of A1 estimator than K estimator for samples smaller than 256, and only slightly worse for larger samples. Keeping in perspective the computational complexity of the K estimator, we can conclude that the A1 estimator is also a better choice for the SC polarimetric case. Finally, overall both the mono-pol estimators perform very poorly, with the exception of N estimator performing reasonably well only for the  $\omega$  parameter.

### IX. GOODNESS OF FIT USING LOG CUMULANTS

A specialized GoF statistic, based on multiple LCs, has been recently developed for PolSAR distributions [31]. Traditionally, GoF testing has been performed by assessing the fitting of intensity or amplitude pdfs to data histogram for each channel separately. GoF using LCs offers a truly multivariate approach, where a single test statistic is obtained for the multivariate PolSAR data. Further, it captures more statistical information by performing GoF using multiple LCs. In the following, we briefly list the most relevant results for the simple hypothesis case, where the model parameters are considered known (for details see [31]).

Let  $\langle \kappa \rangle$  be a  $p$  dimensional vector of sample MLCs of selected orders  $\{v_1, v_2, \dots, v_p\}$ :

$$\langle \kappa \rangle = [\langle \kappa_{v_1} \rangle, \langle \kappa_{v_2} \rangle, \dots, \langle \kappa_{v_p} \rangle]^T, \quad (70)$$

with mean vector  $\kappa$ :

$$\mathbf{E}\{\langle \kappa \rangle\} = \kappa = [\kappa_{v_1}, \kappa_{v_2}, \dots, \kappa_{v_p}]^T. \quad (71)$$

It was shown in [31] that for sample size  $n$ :

$$\sqrt{n}(\langle \kappa \rangle - \kappa) \xrightarrow{\mathcal{D}} \mathcal{N}_p(\mathbf{0}, \mathbf{K}) \quad (72)$$

where  $\mathbf{K}$  is the scaled covariance matrix, given by:

$$\mathbf{K} = n\mathbf{E}\{(\langle \kappa \rangle - \kappa)(\langle \kappa \rangle - \kappa)^T\}. \quad (73)$$

The mean vector  $\kappa$  is formed using the corresponding  $p$  population MLCs of the hypothesized model, and the  $\mathbf{K}$  matrix requires MLCs up to order  $2v_{\max} = 2 \cdot \max\{v_1, v_2, \dots, v_p\}$ . The equation to construct  $\mathbf{K}$  matrix using MLCs up to order  $2v_{\max}$  is given in the appendix of [31].

We can define a test statistic,  $Q_p$ , which uses  $p$  sample MLCs:

$$Q_p = n(\langle \kappa \rangle - \kappa)^T \mathbf{K}^{-1} (\langle \kappa \rangle - \kappa) \quad (74)$$

It readily follows from the multinormal assumption:

$$Q_p \xrightarrow{\mathcal{D}} \chi^2(p) \quad (75)$$

where  $\chi^2(p)$  denotes the  $\chi^2$  distribution with  $p$  degrees of freedom. Therefore, a test with a certain significance level can be constructed and the  $p$  value can be computed. We have also utilized the same theory to compute GoF for the SC polarimetric case. In this case sample MLCs are replaced by sample LCs of the FP-PWF, the rest of the theory remains the same.

One important remark should be made. The number of MLCs required by GoF test is at least one more than the number of texture shape parameters. Thus, for the  $\mathcal{G}$  distribution (two shape parameters) we utilize second, third, and fourth MLCs and, therefore require up to order eight MLCs to construct the  $\mathbf{K}$  matrix. This also explains why we computed GIG LCs upto the eighth order. Finally, higher order LCs have higher variance, therefore the relative error of order  $10^{-4}$ , for the eighth GIG LC, is considered acceptable for GoF testing.

### X. APPLICATION TO REAL DATA

We have statistically analyzed two PolSAR images acquired using TerraSAR-X experimental quad-pol mode. The first image is over Amsterdam, which has been multilooked to have 7.5 equivalent number of looks. The second one is a singlelook image over Barcelona. Note that for both images, the results are organized in a way very similar to [31] for consistency, ease of comparison and clarity.

Figure 4 and 5 show the statistical analysis on Amsterdam and Barcelona images, respectively. In both cases the first row presents a carefully chosen subset image, which has a variety of different types of areas. The image subsets are displayed in false color using the well known Pauli decomposition [52]. From these subset images four square areas are extracted, each of size  $16 \times 16$  pixels. The selection process is shown as tiny color-coded squares in the top row subset images. In the middle row, the color-coded squares expand to show zoomed sample images. The sample images are selected carefully such that they are as homogeneous as possible so as to keep the statistics stationary. The bottom row shows sample LCs obtained from each extracted area and plotted using '+' symbol in texture LC diagram. It also shows multiple color-coded bootstrapped sample LCs plotted for each sample image. These are obtained by collecting 128 bootstrap samples (using sampling with replacement [53]) each of size 128 from the 256-pixel sample images. We also show 95% confidence ellipses drawn using  $2 \times 2$   $\mathbf{K}$  matrices, which are computed by utilizing sample LCs up to the fourth order<sup>10</sup> (see [10], [31]). This gives a good idea of the statistical variation of sample LCs for each extracted sample image.

We have also fitted  $\mathcal{K}$ ,  $\mathcal{G}^0$ , and Kummer- $\mathcal{U}$  distributions to the sample images apart from the  $\mathcal{G}$  distribution. In this way, we can compare the fitting of  $\mathcal{G}$  distribution to the less flexible  $\mathcal{K}$  and  $\mathcal{G}^0$  distributions, and also to the Kummer- $\mathcal{U}$  distribution

<sup>10</sup>Note that appropriate scaling by  $\frac{1}{d^v}$  needs to be taken into account when converting sample MLCs to sample texture LCs, and also in the calculation of  $\mathbf{K}$  matrices.



as it has similar representation in the LC diagram. For  $\mathcal{G}$  distribution we have used the A1, F, N, and K estimators. We should emphasize that the GoF using LCs is also computed for F, N and K estimators, although they are not based on MKS. Consequently, we expect low p values for these estimators. For  $\mathcal{K}$ ,  $\mathcal{G}^0$ , and Kummer- $\mathcal{U}$ , in addition to the A1 estimator, we have also used the so called A2 estimator. It must be noted that the A1 and A2 estimators for Kummer- $\mathcal{U}$  model are only utilized in the MC polarimetric case as this is sufficient for comparing the modeling flexibility of  $\mathcal{G}$  and Kummer- $\mathcal{U}$  distributions. Let us list these additional estimators before GoF analysis.

The A1 estimators for  $\mathcal{K}$ ,  $\mathcal{G}^0$ , and Kummer- $\mathcal{U}$  distributions for MC polarimetric data are given by [29]:

$$\kappa_{v>1}\{\mathbf{C}\} = d^v \psi^{(v-1)}(\hat{\xi}) + \psi_d^{(v-1)}(L), \quad (76)$$

$$\kappa_{v>1}\{\mathbf{C}\} = (-d)^v \psi^{(v-1)}(\hat{\zeta}) + \psi_d^{(v-1)}(L), \quad (77)$$

$$\kappa_{v>1}\{\mathbf{C}\} = d^v \left( \psi^{(v-1)}(\hat{\xi}) + (-1)^v \psi^{(v-1)}(\hat{\zeta}) \right) + \psi_d^{(v-1)}(L), \quad (78)$$

respectively, where  $v=2$  for  $\mathcal{K}$ , and  $\mathcal{G}^0$ , while  $v=2, 3$  for Kummer- $\mathcal{U}$  model, and  $\xi, \zeta > 0$  are the shape parameters. In SC polarimetric case, the A1 estimators for  $\mathcal{K}$  and  $\mathcal{G}^0$  distributions are given by:

$$\kappa_{v>1}\{y\} = \psi^{(v-1)}(\hat{\xi}) + \kappa_{v>1}\{Q\}, \quad (79)$$

$$\kappa_{v>1}\{y\} = (-1)^v \psi^{(v-1)}(\hat{\zeta}) + \kappa_{v>1}\{Q\}, \quad (80)$$

respectively, where  $v=2$  and  $\xi, \zeta > 0$  are again the shape parameters.

The A2 estimator for  $\mathcal{K}$ , and  $\mathcal{G}^0$  distributions can be directly deduced from (74) in Section IX. Its general form usable for  $\mathcal{K}$ , and  $\mathcal{G}^0$  distributions is given by [31]:

$$\hat{\theta} = \arg \left\{ \min_{\theta} \left\{ (\langle \kappa \rangle - \kappa)^T \mathbf{K}^{-1} (\langle \kappa \rangle - \kappa) \right\} \right\}, \quad (81)$$

where  $\theta$  is the vector of texture shape parameters (only one in this case) and  $\langle \kappa \rangle = [\langle \kappa_2 \rangle, \langle \kappa_3 \rangle]$ . The squared Mahalanobis distance is minimized by changing  $\kappa$  and  $\mathbf{K}$ , both of which depend on  $\theta$  through theoretical LCs. A three dimensional A2 estimator for the  $\mathcal{G}$ , and Kummer- $\mathcal{U}$  distributions, using second, third, and fourth LCs, can also be defined but this will require up to the eighth order LCs to form the  $\mathbf{K}$  matrix at each iteration of the minimizer. We have refrained from using such an estimator due to its computational complexity. However, two dimensional A2 estimators (81) can also be defined for the  $\mathcal{G}$ , and Kummer- $\mathcal{U}$  distributions. These are based on the fact that within the GIG/Fisher texture LC domain, these estimators reduce to the corresponding A1 estimators. Outside this domain, they simply reduce to the A2 estimator for either  $\mathcal{K}$  or  $\mathcal{G}^0$  distribution depending on the sign of third texture LC,  $\kappa_3\{\tau\}$ .

Table III shows the p values (%) of GoF tests obtained for the different model-estimators over sample images from MC Amsterdam and SC Barcelona data sets<sup>11</sup>. For both data sets, we have selected one water sample (orange), one

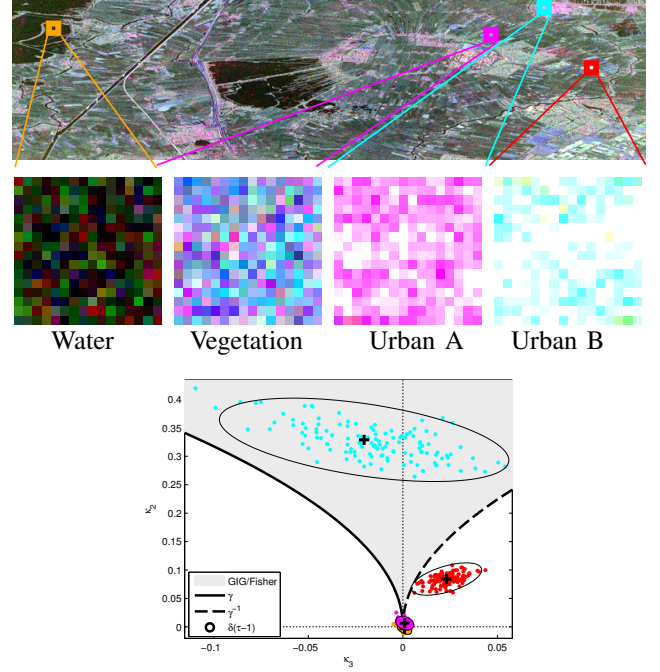


Fig. 4. (Top) A portion of TerraSAR-X polarimetric image over Amsterdam (7.5 equivalent number of looks) shown in false color Pauli decomposition © DLR 2012 . (Middle) Four sample images extracted over different homogeneous areas. (Bottom) Texture log cumulant diagram showing sample log cumulants and color-coded bootstrapped samples of the extracted areas.

vegetation sample (magenta), and two urban samples, urban A (cyan) and urban B (red). The corresponding sample LCs and bootstrapped samples (color matched) are shown in the texture LC diagram in the bottom row of each figure.

Let us first analyze the results on Amsterdam data set. The texture LCs of the water sample are almost completely covered by those of the vegetation sample. However, both of them show gaussian behaviour as they are very close to the black circle. In both the cases, we see that only  $\mathcal{G}_F$ ,  $\mathcal{G}_N$ , and  $\mathcal{G}_K$  fail the test at 5% significance level, while  $\mathcal{G}_{A2}$ ,  $\mathcal{G}_{A2}^0$ , and  $\mathcal{U}_{A2}$  show the highest p values (84.82% for water sample and 89.60% for vegetation). All the remaining model-estimators show smaller but similarly very high p values. Urban B sample shows texture behaviour outside the  $\gamma^{-1}$  manifold. Again  $\mathcal{G}_F$ ,  $\mathcal{G}_N$ , and  $\mathcal{G}_K$  fail the 5% significance test, but this time  $\mathcal{K}_{A1}$ ,  $\mathcal{K}_{A2}$ , and also  $\mathcal{U}_{A1}$  (4.73%) fail this test. This is intuitive for  $\mathcal{K}_{A1}$ , and  $\mathcal{K}_{A2}$  since the sample LCs lie on the opposite side of the  $\gamma$  manifold, but unexpected for  $\mathcal{U}_{A1}$ . All the remaining cases pass this test with  $\mathcal{G}_{A2}$ ,  $\mathcal{G}_{A2}^0$ , and  $\mathcal{U}_{A2}$  sharing the highest p value of 20.71%. The p values are equal because outside the GIG/Fisher texture boundary on  $\gamma^{-1}$  side,  $\mathcal{G}_{A2}$ , and  $\mathcal{U}_{A2}$  reduce to  $\mathcal{G}_{A2}^0$ . Interestingly, it can be noticed that  $\mathcal{U}_{A1}$  (4.73%) performs worse than  $\mathcal{G}_{A1}$ , and  $\mathcal{G}_{A1}^0$  (16.86%). This can be easily explained as, unlike  $\mathcal{U}_{A2}$ ,  $\mathcal{U}_{A1}$  suffers from over-fitting when sample LC falls outside the GIG/Fisher LC domain. Theoretically  $\mathcal{G}_{A1}$  should also suffer from the same over-fitting, but it does not as we estimate only  $\alpha$  (assuming  $\omega=10^{-6}$ ) whenever sample LCs fall outside the GIG/Fisher domain. Finally, Urban A shows a good example of sample LCs falling inside the GIG/Fisher LC domain. In this case both  $\mathcal{G}_{A1}$  and

<sup>11</sup>Different estimators for each model are symbolically represented in the subscript in table III.

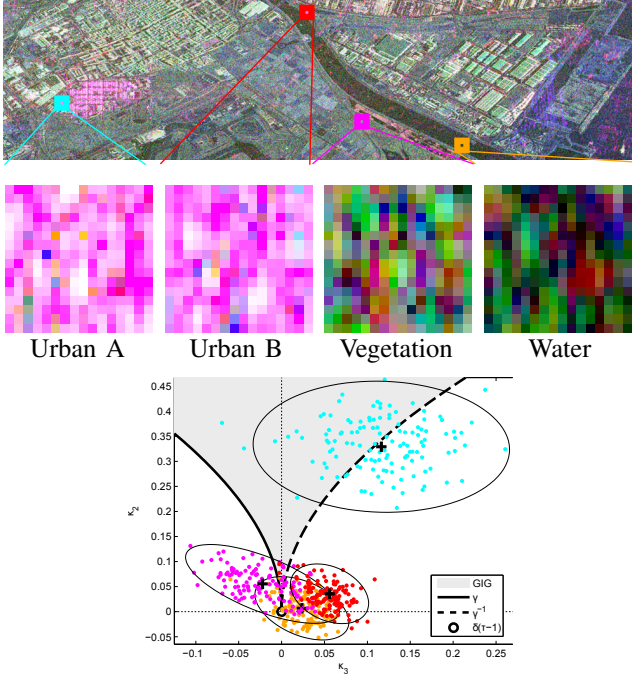


Fig. 5. (Top) A portion of TerraSAR-X singlelook polarimetric image over Barcelona shown in false color Pauli decomposition © DLR 2012. (Middle) Four sample images extracted over different homogeneous areas. (Bottom) Texture log cumulant diagram showing sample log cumulants and color-coded bootstrapped samples of the extracted areas.

$\mathcal{G}_{A2}$  show the highest p value of 84.28%, while  $\mathcal{G}_F$ ,  $\mathcal{G}_N$ ,  $\mathcal{G}_K$ ,  $\mathcal{G}_{A1}^0$ , and  $\mathcal{G}_{A2}^0$  fail the 5% significance test. It is also observed that  $\mathcal{K}_{A1}$ , and  $\mathcal{K}_{A2}$  both pass the test with relatively higher p values of 20.49% and 30.48%, respectively. Interestingly, although both  $\mathcal{U}_{A1}$ , and  $\mathcal{U}_{A2}$  pass the test with a p value of 58.85%, it is less than the p value of 84.28% shared between  $\mathcal{G}_{A1}$  and  $\mathcal{G}_{A2}$ .

Let us now analyze the results obtained on Barcelona data set. The water sample again shows gaussian characteristics and all the model-estimators easily pass the 5% significance level test except  $\mathcal{G}_N$ . In fact,  $\mathcal{G}_N$  fails the test for all the samples examined, and hence has been omitted from further analysis. As the water sample LCs fall slightly outside the GIG LC domain on the  $\gamma^{-1}$  side, the highest p value of 94.44% is shown by both  $\mathcal{G}_{A2}$  and  $\mathcal{G}_{A2}^0$ . The lowest p value of 73.98% is exhibited by  $\mathcal{G}_F$ . The vegetation sample LC falls outside the  $\gamma$  side of the GIG LC domain. The highest p value of 85.71% is, therefore, given by  $\mathcal{G}_{A2}$  and  $\mathcal{K}_{A2}$ . Again, all the model-estimators pass the test, with  $\mathcal{G}_F$  performing the worst. The sample texture LCs of Urban B sample show  $\beta^{-1}$  texture behaviour. All the model-estimators, except  $\mathcal{G}_F$ , still pass the test. The highest p value of 63.23% is shown by both  $\mathcal{G}_{A2}$  and  $\mathcal{G}_{A2}^0$ . Finally, for urban A sample both  $\mathcal{K}_{A1}$  and  $\mathcal{K}_{A2}$  fail the test since it shows sample LCs around  $\gamma^{-1}$  manifold. The highest p value of 91.56% is shown by both  $\mathcal{G}_{A2}$  and  $\mathcal{G}_{A2}^0$  followed closely by  $\mathcal{G}_{A1}$  and  $\mathcal{G}_{A1}^0$ , while  $\mathcal{G}_F$  fails the test.

We can draw a few important inferences from GoF analysis on real data. In SC polarimetric case,  $\mathcal{G}_{A2}$  performs the best, followed closely by  $\mathcal{G}_{A1}$ ,  $\mathcal{G}_{A2}^0$ , and  $\mathcal{G}_{A1}^0$ . For MC polarimetric case, again  $\mathcal{G}_{A2}$  performs the best, followed by  $\mathcal{U}_{A2}$ ,  $\mathcal{G}_{A1}$ , and

TABLE III  
P VALUES (%) OVER IMAGE SAMPLES EXTRACTED FROM SC BARCELONA AND MC AMSTERDAM TERRASAR-X DATA SETS.

	Urban A		Urban B		Vegetation		Water	
	SC	MC	SC	MC	SC	MC	SC	MC
$\mathcal{G}_{A1}$	91.45	84.28	48.72	16.86	81.99	87.75	87.56	84.07
$\mathcal{G}_{A2}$	91.56	84.28	63.23	20.71	85.71	89.60	94.44	84.82
$\mathcal{G}_F$	0	0.18	0.67	0	19.44	0	73.98	0
$\mathcal{G}_N$	0	0.09	0	0	0	0	0	0
$\mathcal{G}_K$	91.25	0.09	10.15	2.88	84.76	1.04	93.38	2.04
$\mathcal{G}_{A1}^0$	91.30	0.83	41.60	16.86	73.29	87.75	87.46	84.07
$\mathcal{G}_{A2}^0$	91.56	3.60	63.23	20.71	79.18	89.60	94.44	84.82
$\mathcal{K}_{A1}$	0.61	20.49	36.59	0.01	83.25	85.55	87.14	84.07
$\mathcal{K}_{A2}$	0.61	30.48	36.59	0.23	85.71	87.27	86.89	84.82
$\mathcal{U}_{A1}$	-	58.85	-	4.73	-	88.38	-	84.82
$\mathcal{U}_{A2}$	-	58.85	-	20.71	-	89.60	-	84.82

$\mathcal{U}_{A1}$ . In fact, in this case, the highest p value is also shared by  $\mathcal{U}_{A2}$  in three of the four extracted samples. This is substantial evidence that the modeling flexibility of  $\mathcal{G}$ , and Kummer- $\mathcal{U}$  distributions is very similar, and intuitively understandable by their common representation in the LCs diagram.

Finally, we can comment about the computation times of different model-estimators on real data. Table IV lists these for all the model-estimators on extracted samples of MC polarimetric Amsterdam data. The  $\mathcal{K}$ , and  $\mathcal{G}^0$  model-estimators are the fastest because they have only one texture parameter. Amongst the  $\mathcal{G}$  model-estimators  $\mathcal{G}_{A1}$  and  $\mathcal{G}_{A2}$  are generally the fastest except for urban A sample. The  $\mathcal{G}$  model-estimators also generally appear to be faster than Kummer- $\mathcal{U}$  model-estimators. However, a closer look reveals that  $\mathcal{U}$  model-estimators are actually faster inside the GIG/Fisher domain (urban A sample). Outside this domain (urban B, vegetation, and water samples) only one texture shape parameter, i.e.  $\alpha$  (assuming  $\omega=10^{-6}$ ), was estimated for  $\mathcal{G}$  model, while both texture shape parameters were estimated for the Kummer- $\mathcal{U}$  model. This explains the seemingly slower computation time of Kummer- $\mathcal{U}$  estimators.

## XI. CONCLUSION

The polarimetric  $\mathcal{G}$  distribution has been explored in the light of state-of-the-art Mellin kind statistics for PolSAR data. We have derived closed form expressions for the Mellin kind characteristic function, cumulant generating function, and log cumulants of generalized inverse gaussian distribution. It has also been shown that log cumulants of this distribution up to the eighth order can be accurately computed using numerical differentiation. We have also derived closed form expressions for the log cumulants of  $\mathcal{G}$  distribution under multilook intensity, singlelook polarimetric, and multilook polarimetric cases of the product model. The estimators derived by employing the method of log cumulants have been rigorously compared with existing estimators using simulated PolSAR data. Generally, improvement in bias, variance, and mean squared error has been reported for the new estimators on synthetic data, along with a competitive computation time. On real data, state-of-the-art GoF testing, using log cumulants, has been utilized to compute the GoF of new and old estimators. This has also been compared to GoF of  $\mathcal{K}$ ,  $\mathcal{G}^0$ , and Kummer- $\mathcal{U}$  distributions

TABLE IV  
COMPUTATION TIME (MILLISECONDS) OF ESTIMATION ON IMAGE  
SAMPLES EXTRACTED FROM MC AMSTERDAM TERRASAR-X DATA.

	Urban A	Urban B	Vegetation	Water
$\mathcal{G}_{A1}$	137.5	11.3	23.8	30.4
$\mathcal{G}_{A2}$	137.5	16.3	19.0	18.8
$\mathcal{G}_F$	46.7	58.4	91.0	134.2
$\mathcal{G}_N$	390.4	370.0	167.5	205.3
$\mathcal{G}_K$	45.6	44.3	31.1	57.3
$\mathcal{G}_{A1}^0$	5.8	11.2	25.8	26.2
$\mathcal{G}_{A2}^0$	12.3	16.3	18.1	18.9
$\mathcal{K}_{A1}$	5.7	11.3	17.0	29.8
$\mathcal{K}_{A2}$	15.4	15.5	17.3	17.7
$\mathcal{U}_{A1}$	8.7	106.5	87.0	53.7
$\mathcal{U}_{A2}$	8.7	141.1	134.4	168.2

on real data. It can be confirmed that with the new estimators, the  $\mathcal{G}$  distribution can not only mimic the modeling flexibility of  $\mathcal{K}$ ,  $\mathcal{G}^0$ , and Kummer- $\mathcal{U}$  distributions, but can also compete well in terms of estimator computation time.

In the future, we will utilize the  $\mathcal{G}$  distribution with its new estimators in various PolSAR image analysis algorithms like supervised and unsupervised classification, segmentation, and target detection from background clutter.

#### ACKNOWLEDGMENT

The authors would like to extend their gratitude to Stian Norman Anfinnsen and Anthony Paul Doulgeris, from the University of Tromsø, for their valuable comments and advice. Also, insightful comments from Alejandro César Frery, from Universidade Federal de Alagoas, are appreciated. Finally, we would like to thank the German Aerospace Centre (DLR) for providing the data sets under proposal LAN0963.

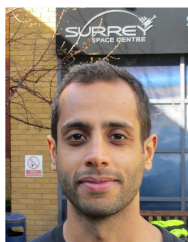
#### REFERENCES

- [1] L. Allen and D. G. C. Jones, "An analysis of the granularity of scattered optical maser light," *Phys. Lett.*, vol. 7, pp. 321–323, Dec. 1963.
- [2] J. W. Goodman, "Some fundamental properties of speckle," *J. Opt. Soc. Am.*, vol. 66, no. 11, pp. 1145–1150, Nov. 1976.
- [3] J.-S. Lee and E. Pottier, *Polarimetric Radar Imaging: From Basics to Applications*. Boca Raton, FL: CRC Press, Taylor & Francis Group, 2009, ch. 4, pp. 101–142.
- [4] C. Oliver and S. Quegan, *Understanding Synthetic Aperture Radar Images*, 2nd ed. Raleigh, NC: SciTech Publishing, 2004.
- [5] A. Lopès, R. Garello, and S. L. Hegarat-Masclé, *Processing of Synthetic Aperture Radar Images*. London, U.K.: John Wiley & Sons, 2008, ch. 5, pp. 87–142.
- [6] A. Frery, H.-J. Muller, C. Yansse, and S. Sant'Anna, "A model for extremely heterogeneous clutter," *IEEE Trans. Geosci. Remote Sens.*, vol. 35, no. 3, pp. 648–659, May 1997.
- [7] C. Tison, J.-M. Nicolas, F. Tupin, and H. Maitre, "A new statistical model for Markovian classification of urban areas in high-resolution SAR images," *IEEE Trans. Geosci. Remote Sens.*, vol. 42, no. 10, pp. 2046–2057, Oct. 2004.
- [8] C. Oliver, "Rain forest classification based on SAR texture," *IEEE Trans. Geosci. Remote Sens.*, vol. 38, no. 2, pp. 1095–1104, Mar 2000.
- [9] T. Eltoft and K. Hogda, "Non-gaussian signal statistics in ocean SAR imagery," *IEEE Trans. Geosci. Remote Sens.*, vol. 36, no. 2, pp. 562–575, Mar. 1998.
- [10] T. Eltoft, S. Anfinnsen, and A. Doulgeris, "A multitexture model for multilook polarimetric radar data," in *Proc. IGARSS*, Vancouver, BC, Jul. 2011, pp. 1048–1051.
- [11] S. Khan and R. Guida, "The new dual-texture  $\mathcal{G}$  distribution for single-look PolSAR data," in *Proc. IGARSS*, Munich, Germany, Jul. 2012, in press.
- [12] N. R. Goodman, "Statistical analysis based on a certain multivariate complex Gaussian distribution (an introduction)," *Ann. Math. Statist.*, vol. 34, no. 1, pp. 152–177, Mar. 1963.
- [13] H. H. Lim, A. A. Swartz, H. A. Yueh, J. A. Kong, R. T. Shin, and J. J. van Zyl, "Classification of earth terrain using polarimetric Synthetic Aperture Radar images," *J. Geophys. Res.*, vol. 94, no. B6, pp. 7049–7057, 1989.
- [14] J. Lee, M. Grunes, and R. Kwok, "Classification of multi-look polarimetric SAR data based on complex Wishart distribution," *Int. J. Remote Sensing*, vol. 15, no. 11, pp. 2299–2311, 1994.
- [15] J.-M. Nicolas, "Introduction aux statistique de deuxième espèce: Application des logs-moments et des logs-cumulants à l'analyse des lois images radar," *Traitement du Signal*, vol. 19, no. 3, pp. 139–167, Jun. 2002, in French.
- [16] —, "Application de la transformée de mellin: Étude des lois-statistiques de l'imagerie cohérente," Ecole Nationale Supérieure des Télécommunications, Tech. Rep., 2006D010, in French.
- [17] F. Galland, J.-M. Nicolas, H. Sportouche, M. Roche, F. Tupin, and P. Réfrégier, "Unsupervised synthetic aperture radar image segmentation using Fisher distributions," *IEEE Trans. Geosci. Remote Sens.*, vol. 47, no. 8, pp. 2966–2972, 2009.
- [18] S. Quegan, I. Rhodes, and R. Caves, "Statistical models for polarimetric SAR data," in *Proc. IGARSS*, vol. 3, Pasadena, CA, Aug. 1994, pp. 1371–1373.
- [19] J. Lee, D. Schuler, R. Lang, and K. Ranson, "K-distribution for multi-look processed polarimetric SAR imagery," in *Proc. IGARSS*, vol. 4, Pasadena, CA, Aug. 1994, pp. 2179–2181.
- [20] S. H. Yueh, J. A. Kong, J. K. Jao, R. T. Shin, and L. M. Novak, "K-distribution and polarimetric terrain radar clutter," *J. Electrom. Waves Appl.*, vol. 3, pp. 747–768, Aug. 1989.
- [21] C. Freitas, A. Frery, and A. Correia, "The polarimetric  $\mathcal{G}$  distribution for SAR data analysis," *Environmetrics*, vol. 16, no. 1, pp. 13–31, Feb. 2005.
- [22] L. Bombrun and J.-M. Beaulieu, "Fisher distribution for texture modeling of polarimetric SAR data," *IEEE Trans. Geosci. Remote Sens.*, vol. 5, no. 3, pp. 512–516, Jul. 2008.
- [23] L. Bombrun, G. Vasile, M. Gay, and F. Totir, "Hierarchical segmentation of polarimetric SAR images using heterogeneous clutter models," *IEEE Trans. Geosci. Remote Sens.*, vol. 49, no. 2, pp. 726–737, Feb. 2011.
- [24] L. Bombrun, S. Anfinnsen, and O. Harant, "A complete coverage of log-cumulant space in terms of distributions for polarimetric SAR data," in *Proc. PolInSAR*, Frascati, Italy, 2011.
- [25] S. Khan and R. Guida, "On single-look multivariate  $\mathcal{G}$  distribution for PolSAR data," *IEEE J. Sel. Topics Appl. Earth Observations Remote Sens.*, vol. 5, no. 4, pp. 1149–1163, Aug. 2012.
- [26] H.-J. Muller and R. Pac, "G-statistics for scaled SAR data," in *Proc. IGARSS*, vol. 2, Hamburg, Germany, Jul. 1999, pp. 1297–1299.
- [27] A. C. Frery, J. Jacobo-Berlles, J. Gambini, and M. Mejail, "Polarimetric SAR image segmentation with B-splines and a new statistical model," *Multidimensional Syst. Signal Process.*, vol. 21, no. 4, pp. 319–342, Dec. 2010.
- [28] A. Doulgeris and T. Eltoft, "Scale mixture of Gaussians modelling of polarimetric SAR data," *EURASIP J. Adv. Signal Process.*, vol. 2010, no. 874592, pp. 1–12, Jan. 2010.
- [29] S. Anfinnsen and T. Eltoft, "Application of the matrix-variate Mellin transform to analysis of polarimetric radar images," *IEEE Trans. Geosci. Remote Sens.*, vol. 49, no. 6, pp. 2281–2295, Jun. 2011.
- [30] S. Anfinnsen, "On the supremacy of logging," in *Proc. PolInSAR*, Frascati, Italy, 2011.
- [31] S. Anfinnsen, A. Doulgeris, and T. Eltoft, "Goodness-of-fit tests for multilook polarimetric radar data based on the Mellin transform," *IEEE Trans. Geosci. Remote Sens.*, vol. 49, no. 7, pp. 2764–2781, Jul. 2011.
- [32] K. Tragl, "Polarimetric radar backscattering from reciprocal random targets," *IEEE Trans. Geosci. Remote Sens.*, vol. 28, no. 5, pp. 856–864, Sep. 1990.
- [33] S. Anfinnsen, "Statistical analysis of multilook polarimetric radar images with Mellin transform," Ph.D. dissertation, University of Tromsø, Tromsø, May 2010, chapter 2, Section 2.2.4.
- [34] A. M. Mathai, *Jacobians of Matrix Transformations and Functions of Matrix Argument*. New York: Springer-Verlag, 1997, ch. 6.
- [35] L. Andrews and R. Phillips, *Mathematical Techniques for Engineers and Scientists*. New Delhi-110001: Prentice-Hall of India, 2005, ch. 13.
- [36] N. Johnson, S. Kotz, and N. Balakrishnan, *Continuous Univariate Distributions*, 2nd ed. New York: John Wiley & Sons, Inc., 1994, vol. 1, ch. 15.

- [37] B. Jørgensen, *Statistical Properties of the Generalized Inverse Gaussian Distribution (Lecture Notes in Statistics)*. New York: World Scientific, 1982, vol. 9.
- [38] F. Pascal, P. Forster, J.-P. Ovarlez, and P. Larzabal, "Performance analysis of covariance matrix estimates in impulsive noise," *IEEE Trans. Signal Process.*, vol. 56, no. 6, pp. 2206–2217, Jun. 2008.
- [39] F. Gini and M. Greco, "Covariance matrix estimation for CFAR detection in correlated heavy tailed clutter," *Signal Process.*, vol. 82, no. 12, pp. 1847–1859, Dec. 2002.
- [40] A. Frery, A. Correia, and C. da Freitas, "Classifying multifrequency fully polarimetric imagery with multiple sources of statistical evidence and contextual information," *IEEE Trans. Geosci. Remote Sens.*, vol. 45, no. 10, pp. 3098–3109, Oct. 2007.
- [41] A. Frery, F. Cribari-Neto, and M. Souza, "Analysis of minute features in speckled imagery with maximum likelihood estimation," *EURASIP J. Appl. Signal Process.*, vol. 2004, no. 16, pp. 2476–2491, Jan. 2004.
- [42] K. L. P. Vasconcellos, A. C. Frery, and L. B. Silva, "Improving estimation in speckled imagery," *Computational Statistics*, vol. 20, no. 3, pp. 503–519, 2005.
- [43] F. Cribari-Neto, A. C. Frery, and M. F. Silva, "Improved estimation of clutter properties in speckled imagery," *Computational Statistics and Data Analysis*, vol. 40, no. 4, pp. 801–824, 2002.
- [44] L. Novak, M. Burl, and W. Irving, "Optimal polarimetric processing for enhanced target detection," *IEEE Trans. Aerosp. Electron. Syst.*, vol. 29, no. 1, pp. 234–244, Jan 1993.
- [45] A. Stuart and J. Ord, *Kendall's Advanced Theory of Statistics: Distribution Theory*, 6th ed. New York: John Wiley & Sons Inc., 1994, vol. 1.
- [46] A. R. Hall, *Generalized Method of Moments*, 6th ed. Oxford, U.K.: Oxford University Press, 2005.
- [47] S. Anfinson, A. Doulgeris, and T. Eltoft, "Estimation of the equivalent number of looks in polarimetric synthetic aperture radar imagery," *IEEE Trans. Geosci. Remote Sens.*, vol. 47, no. 11, pp. 3795–3809, Nov. 2009.
- [48] J. Lyness and C. Moler, "Van der Monde systems and numerical differentiation," *Numer. Math.*, vol. 8, pp. 458–464, 1966.
- [49] —, "Generalized Romberg methods for integrals of derivatives," *Numer. Math.*, vol. 14, pp. 1–13, 1969.
- [50] J. D'Errico. (2011) Adaptive robust numerical differentiation. <http://www.mathworks.co.uk/matlabcentral/fileexchange/13490-adaptive-robust-numerical-differentiation>. Accessed 26 Mar. 2013.
- [51] —. (2007) Derivest. <http://convexoptimization.com/TOOLS/DERIVEST.pdf>. Accessed 26 Mar. 2013.
- [52] J.-S. Lee and E. Pottier, *Polarimetric Radar Imaging: From Basics to Applications*. Boca Raton, FL: CRC Press, Taylor & Francis Group, 2009.
- [53] B. Efron and R. Tibshirani, *An Introduction to the Bootstrap*, ser. Monographs on Statistics & Applied Probability. Chapman & Hall, 1993, ch. 6, pp. 45–59.



**Raffaella Guida** (S'04–M'08) was born in Naples, Italy, on October 24, 1975. She received the Laurea degree (cum laude) in Telecommunications Engineering and the Ph.D. degree in Electronic and Telecommunications Engineering from the University of Naples Federico II, Naples, in 2003 and 2007, respectively. In 2003, she received a grant from the University of Naples Federico II to be spent at the Department of Electronic and Telecommunication Engineering (DIET) for research in the field of remote sensing. In 2006, she received a two-year grant from the University of Naples Federico II to be spent at DIET for research in electromagnetics, particularly on the topic of electromagnetic field propagation in an urban environment, within the Italian project S.Co.P.E. aimed to develop a distributed high-performance system for multidisciplinary scientific elaborations. In 2006, she was also a Guest Scientist with the Department of Photogrammetry and Remote Sensing, Technische Universität München, München, Germany. In 2008, she joined the Surrey Space Centre (SSC), University of Surrey, Guildford, U.K., as Lecturer in Satellite Remote Sensing. Today she is still in SSC where she leads the Remote Sensing Applications group. Her main research interests are in the fields of electromagnetics and microwave remote sensing, particularly in simulation and modeling of synthetic aperture radar signals relevant to natural surfaces and urban scenes, new remote sensing mission concepts and applications. She is involved as PI and co-I in many national and European research projects.



**Salman Khan** (S'11) was born in 1982 in Lahore, Pakistan. He received B.S. degree in Computer Sciences from National University of Computer and Emerging Sciences, Pakistan in 2004, the M.S. degree in Electrical Engineering as a Fulbright scholar from University of Central Florida, Orlando, U.S.A. in 2009, and is currently in the fourth year of Ph.D. degree in Electronics Engineering (Remote Sensing Applications group) at the Surrey Space Centre, University of Surrey in Guildford, U.K. His current research interests include Statistical Signal

Processing in polarimetric SAR, and its applications in Pattern Recognition and Target Detection.

He is the recipient of IEEE GRSS 2013 J-STARS Prize Paper Award for the paper titled *On Single-Look Multivariate G Distribution for PolSAR Data*.